

Romain JAN
romain.jan@isae-sup Aero.fr

Experimental validation of ASWING. Part III: Structure

Supervisors:

- Prof J-M. Moschetta
- Prof J-P. Condomines

ISAE-Supaero: Technical report, ISAE-ASW-3 2024

Abstract

This technical report presents an experimental validation of the ASWING structural model. In the first section, the models are recalled and detailed. Secondly, the numerical scheme convergence and the computational time for tip deflections and modal response predictions are provided. Thirdly, experimental validations are presented. Large tip deflection on helicopter blades and moderate to low aspect ratio wings are presented. These cases are chosen to highlight both stiffness coupling and aspect ratio limitation. Finally, the modal responses of each case are compared with experiments found within the literature. This technical report also assesses the impact of concentrated masses, such as nacelles or tanks, on a wing modal response. Specifically, it analyses the effects of their position along the chord and span of the wing. Overall, ASWING provides excellent agreements with experiments for tip deflection, twist and modal response for beams with an aspect ratio greater than 6. And so no matter the composite layout, that can involve various bending coupling terms. ASWING captures also well the spanwise and chordwise position effect of the nacelle on the modal response of a wing. Finally, those predictions are provided in less than 0.1 (deflection) and 2.0 seconds (modal response) on modern laptops.

Important note to the reader:

This work has not been peer reviewed yet. Only the author's PhD referee members (Professors Mark Drela, Rafael Palacios, Eric Laurendeau and Murat Bronz) had access to this work and have authorised the defence. For more details, please refer to <https://www.theses.fr/s251420>. Nevertheless, this material is in a process of publication in peer reviewed journals, in a shorter version. This document will be updated if new material has to be added.

About the data presented in this report:

This report presents various comparisons with different sets of experimental data. The latter and numerical simulations are available on demand. However, if you consider using them for your own studies, please cite this work and the related ones from which data are coming. Contact: romain.jan@isae-supraero.fr

Version notes

This technical report aims to be updated if new experimental cases and ASWING modifications have to be added. Also, the updates aim to take into account the feedback of the community (typos, theoretical development mistakes, etc).

Versioning syntax:

The version of this document is given as follows: III.X.y, where III denotes the third part of this experimental evaluation, X and y denote respectively major and minor updates.

- **Version III.1.0:**

(30/07/2023) This version is the one submitted to the author's PhD referee as a partial fulfilment of the PhD degree. This version presented the following experimental cases:

- CASE A: (high aspect ratio) Five helicopter blades, with various composite layouts. Tip displacement and twist predictions, as well as modal response.
- CASE B: (low aspect ratio) 3 wings with various composite layouts. Tip displacement and twist predictions, as well as modal response.
- CASE C: (low aspect ratio) Effect of nacelle lateral and chordwise position on the modal response.

- **Version III.2.0:**

(16/01/2024) Major typos have been corrected. Some experimental validation cases have been added and are summed up as follows:

- CASE B: The Pazy wing bench (moderate aspect ratio) has been used. Tip displacement and twist as well as modal response are discussed. CASE B and C of Version III.1.0 are now CASE C and D of Version III.2.0

- **Version III.2.1:**

(05/02/2024) Tables 3 and 4 have been corrected. Error calculations between predictions and experiments were wrong. For table 4 wrong stiffness parameters have been used. Everything has been corrected.

- **Version III.3.0:**

(7/05/2024) The modifications brought to the document are summarized as follows:

- Cases have been renamed to $\mathcal{ST}-1$ to 5 to match the formalism of the other technical support.
- A table has been added to summarize the cases and their purposes.
- CASE $\mathcal{ST}-5$ has been added. This case is used to validate the beam connection modelisation. A joined wing aircraft static response to various load cases is presented to do so.
- Other typos have been corrected. The out of the plane bending moment distribution predictions are presented to highlight the benefit brought by joined wings configurations.

- **Version III.3.9:**

(10/05/2024) The modifications brought to the document are summarized as follows:

- CASE $\mathcal{ST}-5$ has been extended with a new compliant joint subcase, to show the strong dependency of the structural static response with the joint type. This case also re-strengthen the Aswing validation on joined wing architecture. CASE $\mathcal{ST}-5$ becomes $\mathcal{ST}-5.A$ for the rigid joint, and $\mathcal{ST}-5.B$ for the compliant one.
- Subnames have been added to CASE $\mathcal{ST}-1$, 2 and 3 to better distinguish the different layouts studied. They become in consequence, $\mathcal{ST}-1.A-E$, $\mathcal{ST}-2.A-B$ and $\mathcal{ST}-3.A-C$

- **Version III.4.0:**

(15/05/2024) The modification brought to the document is summarized as follows:

- CASE $\mathcal{ST}-6.A-E$ have been added to assess the column buckling critical load prediction quality of Aswing. The Euler buckling critical load is in particular invoked. An accuracy parameter is proposed to ensure reasonable buckling divergence prediction.

Contents

1	Introduction	9
2	Structural model	10
2.1	Useful coordinate systems	10
2.2	Inertial acceleration	13
2.3	Beam curvatures and strains	13
2.4	Forces and moment equilibrium	16
2.5	Internal forces and moments in non uniform beams	16
2.6	Distributed/ponctual inertial and gravity loads	22
2.7	Beams connections	24
2.8	Discretization of the problem	24
2.9	Structural failure analysis	25
2.10	Column buckling analysis of non uniform beams	25
3	Numerical scheme convergence and time computation	26
4	Experimental Validation	27
4.1	CASE ST-1: Static deflection and modal response of high aspect ratio helicopter blades . . .	27
4.2	CASE ST-2 : Static deflection and modal response on a moderate aspect ratio wing:	33
4.3	CASE ST-3: static deflection and modal response of low aspect ratio wings : boundary case .	36
4.4	CASE ST-4: Effect of a concentrated mass on the modal response of a straight wing	36
4.5	CASE ST-5.A-B: Joined wings	39
4.6	CASE ST-6.A-E Column buckling	44
5	Conclusion:	46
References		48

List of Figures

1	Structural model useful frames	14
2	Earth to body frame transformation sequence	14
3	Body to local frame transformation sequence	14
4	Beam local curvature, simplified case for illustration	15
5	extensional and shear strains illustration	17
6	Forces and moments equilibrium on a beam element	17
7	Non-uniformity of the section material properties	18
8	Non uniform extensional load distribution, lumping on the tension axis	18
9	Non uniform c and n shear loads due to c and n strains. Lumping on the c-shear and s-shear elastic lines	20
10	ASWING vs classical Euler-Bernoulli beam theory: zero curvature	20
11	ASWING vs classical Euler Bernoulli beam theory: loads distribution	20
12	Distributed inertial and gravity loads, vector directions are arbitrary	23
13	Ponctual mass rigidly connected to the local frame (left). Angular momentum of an engine (right), directions of the vectors are arbitrary	24
14	Examples of geometries implementable in ASWING	25
15	Concentrated load on zero length interval captured as perfect discontinuity. Beam constraints imposed at free tip joint and ground attachment	26
16	Buckling principle illustration, and detection through modal analysis	26
17	Structural model numerical scheme performances	28
18	CASE \mathcal{ST} -1: experimental bench description	30
19	CASE \mathcal{ST} -1.A, layout : [0/90]3s ($\Delta_x, \Delta_y, \Delta_z$) predictions against experiments from Minguet 1989	31
20	CASE \mathcal{ST} -1.B, layout : [20/-70/-70/20]2a, tip ($\Delta_x, \Delta_y, \Delta_z$) predictions against experiments from Minguet 1989	31
21	CASE \mathcal{ST} -1.C, layout : [45/0]3s, tip ($\Delta_x, \Delta_y, \Delta_z$) predictions against experiments from Minguet 1989	32
22	CASE \mathcal{ST} -1.D, layout : [45/0]3a ($\Delta_x, \Delta_y, \Delta_z$) predictions againts experiments from Minguet 1989	32
23	CASE \mathcal{ST} -2.A-B: Pazy wing static deflection and twist. ASWING predictions against UM/-NAST (Riso and Cesnik-2023) and experimental data (Avin et al.-2022)	35
24	CASE \mathcal{ST} -3: low aspect ratio wing, static deflection and modal response experimental bench Dunn	37
25	CASE \mathcal{ST} -3.A-C: NACA0012 wing static tip deflection and twist against tip forces and moments : ASWING and Dunn's model comparison with experimental data (Dunn -1992)	38

26	CASE \mathcal{ST} -4: concentrated mass effect bench Runyan and Sewall (1948)	40
27	CASE \mathcal{ST} -4: Concentrated weight effect on the first bending and torsion modes. ASWING predictions against experiments from Runyan and Sewall (1948).	40
28	CASE \mathcal{ST} -5.A: Joined wing, out of plane bending moment ASWING predictions against experiments of Stearman and Lin et al. (1990). Effect of a rigid joint against a cantilever wing. Effect of the load fraction carried by both wings. For figures (c) and (d) experimental data have been extrapolated from the 30 lbs load case.	42
29	CASE \mathcal{ST} -5.B: Joined wing, out of plane bending moment ASWING predictions against experiments of Stearman and Lin et al. (1990). Effect of a link joint against a cantilever wing. Effect of the load fraction carried by both wings. For figures (b) and (c) experimental data have been extrapolated from the 30 lbs load case.	43
30	CASE \mathcal{ST} -6.A-E: Column buckling validation cases, with various cross section. Effect of the effective slenderness ratio KL/r (with $K = 0.5$) on the critical load. Aswing expected predictions performance based on the Euler critical load solution. Experiments are from Niles's technical note.	45

1	Evolution of the classical Euler-Bernoulli beam theory to the ASWING structural model. References to the sections are displayed where the improvements are detailed	12
2	Experimental evaluation cases. $\mathcal{ST} = \mathcal{S}\mathcal{T}$ ructural cases.	29
3	CASE \mathcal{ST} -1.A-E: helicopter blades modal analysis against experiments (Minguet 1989) . . .	34
4	CASE \mathcal{ST} -2.A (skin off): Pazy wing modal response in undeformed and deformed condition. ASWING, UM/NAST (Riso and Cesnik-2023), Sharpy (Goizueta et al.-2022) predictions against experimental data (Avin et al.-2022)	34
5	CASE \mathcal{ST} -3.A-C: NACA0012 straight wing modal analysis Dunn (1992)	37
6	CASE \mathcal{ST} -4: NACA16010 straight wing modal analysis (NC : reported as Not Clear) Runyan and Sewall (1948). Effect of concentrated weights spanwise and chordwise position on the modal response $\epsilon_{fb_1}^- = 5.6 \pm 2.5\%$, $\epsilon_{fb_2}^- = 7.5 \pm 5.3\%$, $\epsilon_{ft}^- = 10.5 \pm 9\%$	47
7	CASE \mathcal{ST} -1: helicopter blades: properties 1/3 Minguet (1989)	51
8	CASE \mathcal{ST} -1: helicopter blades: properties 2/3	51
9	CASE \mathcal{ST} -1: helicopter blades: properties 3/3	51
10	CASE \mathcal{ST} -3: NACA0012 wing stiffness and geometry parameters Dunn (1992)	51
11	CASE \mathcal{ST} -4: NACA16010 wing concentrated weights properties Runyan and Sewall (1948) .	52
12	CASE \mathcal{ST} -4: NACA16010 wing geometry and structural properties Runyan and Sewall (1948)	52

1 Introduction

N order to reduce commercial aircraft fuel burn, the major work related to conceptual design tends to show that higher aspect ratio and lighter wing are ininevitable. Thus highly flexible structures are expected, with large deflections in cruise conditions. The latter will be more likely subject to flutter and their modal response is expected to be very close to the aircraft flight dynamics [1, 5, 29]. With the large deflection comes the problem of flutter onset [23, 43, 44]. It becomes mandatory now to predict the latter phenomena directly during the pre-design loop to ensure a feasible and flyable architecture. Then without loss of generality on the previous comments, new types of architectures are studied such as joined, C, blended and strut wings, distributed and rear-mounted propulsion etc [7, 10, 21, 41, 50, 51]. They all rise new aeroelastic problems, and simple structural models are no longer enough to assess those types. Also floating wingtips are more and more studied as passive gust alleviation devices and rolling performance improvement solutions [9, 25, 26, 27]. Having a structural model capable of capturing their effects is a real asset for the analysis of this type of application.

In light of the previous comments, one-dimensional non-linear beam models remain prevalent in aeronautics [6, 22, 42, 48, 53]. These models hold interest owing to their ability to produce fast analysis with a reasonable level of accuracy. When fast aerodynamic models such as lifting-line or vortex lattice methods are combined with them, a wide range of aeroelastic phenomena can be studied. SharpY (del Carre et al.-2019) , UMNAST (Su and Cesnik-2010), Openaerostruct (Chauhan and Martins-2019) and Aswing (Drela-1999) are framework proposing the coupling of such models. The latter (Aswing) is of interest in this chapter. This software was first introduced in the 1990s by Drela (1990, 1999) as part of Deadalus project and has been then improved in the 2000s (Drela-2008, 2009). The major problem is that ASWING has been evaluated only 6 times [11, 24, 28, 36, 52, 54]. All the 6 articles have evaluated the same features, i.e. flutter speed or gust load predictions. Furthermore, the aircraft considered in these papers were not stress cases of the model as they all had very high aspect ratio wings. In consequence, we have performed a complete experimental evaluation of the model and its various features in 4 main steps. The three main models that are aerodynamics, structure and propellers have been evaluated separately as it is easier to find experimental data from the literature. Also, it is more convenient to do so in order to highlight the critical parameters of each one

of them. Then they were gathered together so that the aeroelastic features could be evaluated. This technical report presents the ASWING structural model evaluation . The latter derives from a nonlinear, unsteady extension of the classical Euler-Bernoulli beam theory. The ASWING structural model is a multi-beam code mainly adapted from Minguet's works (1989). This code can predict the non-linear deflections (large amplitudes) and modal responses of very flexible structures. Beams can be cantilevered to non-inertial frames, connected by constrained or compliant joints. The section properties (stiffness and mass) are spanwise varying. Elastic, tensile, and centre of gravity position can be arbitrarily defined. The unsteady formulation of the Minguet's model is extended with viscous structural damping, adapted from the work of Banks and Wang (1991, 1987). Internal forces and moments are computed based on the strains and curvatures changes, with coupling terms on bending and torsion. Finally, the discrete model captures pure load discontinuities (point masses, engine thrust, struts) through the use of zero-length intervals.

The technical report is built as follows. In section II, the theoretical model is recalled and voluntary illustrated. As ASWING is a multidisciplinary tool that can be used by the control, aerodynamic and structural design community, our effort is to provide an extended understanding of the models than in the technical documentation ([16, 17] where they have been summarized. In section III, The numerical scheme convergence and computational time are assessed to provide the reader with the optimal mesh refinement and computational performances on a modern laptop. Then in section IV, the experimental evaluation of the model with a focus on non-linear large deflections, modal responses and the effect of concentrated masses (nacelle, tank) on them (modal response only). The test cases have been chosen from high to moderate-low aspect ratios in order to clearly identify the limits of the model. Moreover, test cases have been multiplied as some of them are presenting different composite layouts. The latter are used to assess the simplification made in the model (stiffness matrix reduction). Finally, when it was possible, the predictions have been compared to other models from the literature. The experimental data set is based on the work of Minguet (1990b,1990a) for large deflection and modal response of high aspect ratio helicopter blade (CASE ST-1). For moderate aspect ratio, the recent Pazy wing bench of Avin et al.-2022 is also discussed as an intermediate stress test (CASE ST-2). The work of Dunn and Dugundji (1992) has been used for the large deflection and modal response of low aspect ratio rectangular wing (CASE ST-3). Regarding the tank or engine position effect on the modal response of a straight wing, the work of Runyan and Sewall (1948) has been chosen (CASE ST-4). The effect of beam

connection through joints is studied using the work of Lin et al. on the JWRA-Nasa's prototype (CASE ST-5). Then column divergent buckling prediction is discussed in CASE ST-6 using the experimental data of Niles on 5 different beams. All the different parameters used in the simulations have been summarised and translated into the metric systems in the appendix of this report.

2 Structural model

This section proposes to derive the structural model of ASWING. First, useful coordinate systems are introduced with their relative position, velocity, acceleration, etc. Secondly, the inertial acceleration of any point of the structure is derived to be used in the following sections. Thirdly, beam curvature and strains are detailed so that the internal forces and moments introduced in the force equilibrium section can be derived. Fifthly, distributed and punctual inertial and gravitational loads are derived. Finally, the section concludes with comments on beam connections and discretisation of the problem.

2.1 Useful coordinate systems

The ASWING structural model differs from the classical Euler-Bernoulli theory in that the beams are cantilevered on non-inertial frames. In fact, the model has to describe the steady-state and transient structural behaviour of aircraft elements that may be in non-uniform accelerated motion in space. Consequently, to derive the model accurately, 3 frames are required.

Inertial Frame (Earth)

This frame, cantilevered to any point on the Earth's surface, is inertial. Assuming a flat Earth, it is used to provide the position \vec{R}_E , orientation $\vec{\Theta}$, velocity \vec{U} , rotation rate $\vec{\Omega}$, inertial and angular acceleration \vec{a}_0 and $\vec{\alpha}_0$ of the rigid body frame, i.e. the aircraft. The inertial frame axes are denoted as (X, Y, Z) as shown in the figure 1. $\vec{\Theta} = (\Phi, \Theta, \Psi)^T$ defines the rotation sequence to obtain the body frame orientation according to the sequence shown in figure 2. The body to earth axis transformation matrix is given as

follow:

$$[T_E] = \begin{bmatrix} \cos \Psi & \sin \Psi & 0 \\ -\sin \Psi & \cos \Psi & 0 \\ 0 & 0 & 1 \end{bmatrix} \begin{bmatrix} \cos \Theta & 0 & \sin \Theta \\ 0 & 1 & 0 \\ -\sin \Theta & 0 & \cos \Theta \end{bmatrix} \begin{bmatrix} 1 & 0 & 0 \\ 0 & \cos \Phi & \sin \Phi \\ 0 & -\sin \Phi & \cos \Phi \end{bmatrix} \quad (1)$$

The above equation translates the transformation sequence of figure 2, but from right to left. Note that \vec{R}_E in the Earth frame is expressed as $\vec{R}_E = (X_E, Y_E, Z_E)_E^T$, while the velocity vector is expressed in the body frame as $\vec{U} = (U_x, U_y, U_z)_b^T$. The time variation of the position vector is then given by

$$\frac{d\vec{R}_E}{dt} = [T_E]\vec{U}_b \quad (2)$$

From the equation above the absolute acceleration expressed in the earth frame can be expressed as

$$\vec{a}_0 = \frac{d\vec{U}}{dt} + \vec{\Omega} \times \vec{U} \quad (3)$$

The orientation vector $\vec{\Theta}$ is not expressed in the body nor the earth frame as

$\vec{\Theta} = (\Phi \vec{x}, \Theta \vec{Y1}, \Psi \vec{Z})^T$ while the rotation rate vector $\vec{\Omega}$ is expressed in the body frame $(\Omega_x, \Omega_y, \Omega_z)_b^T$. The relation between $\vec{\Omega}$ and $\vec{\theta}$ is given by projecting the vectors \vec{x} , \vec{y} and \vec{z} on x , $Y1$ and Z as follow

$$\frac{d\vec{\Theta}}{dt} = \begin{bmatrix} -1 & \sin \Phi \tan \Theta & -\cos \Phi \tan \Theta \\ 0 & \cos \Phi & \sin \Phi \\ 0 & \sin \Phi / \cos \Theta & -\cos \Phi / \cos \Theta \end{bmatrix} \vec{\Omega} \quad (4)$$

$$= [C_E]\vec{\Omega}$$

where $[C_E]$ is the projection matrix. The latter is invertable. From $\vec{\Omega}$ can be derived the angular acceleration $\vec{\alpha}_0$ as follow :

$$\vec{\alpha}_0 = \frac{d\vec{\Omega}}{dt} \quad (5)$$

This frame is attached to the aircraft (see figure 1, x points to the tail, y to the right wing and z is constructed to ensure a normal frame (right hand rule). The direction of the body frame axis is provided by the transformation sequence derived in the equation 1. Most of the physical variables are derived in this frame. The latter is really useful for evaluating global aerodynamic parameters such as infinite relative airspeed, angle of attack and side slip angle. At least one of the aircraft elements is cantilevered from the body frame, although the use of a rigid pylon (distant

cantilevering) may be considered.

Local frame $(c, s, n)^T$

This frame is placed along the reference line and is very useful to derive the aerodynamic and structural loads and moments. In ASWING its origin can be placed anywhere along the chord line. However, in the next development it is assumed to be fixed at the leading edge of each wing section.

I - Classical Euler-Bernoulli beam theory (CEB)	II - Extended CEB [39]	III - ASWING 5.96
1750	1989	2008
- small deflection - uniform beam - no torsion - flat straight beam (zero curvature) - small torsion - tension and center of gravity axis at the mid chord	- Improvements of I: + large deflection (non linear) §2.3 & §2.5 + bending torsion coupling §2.5 + shear and extensional stress §2.5 + elastic axis at the mid chord + rotating beam + coupled to a blade element theory	- Improvements of II: + Non inertial cantilevering §2.1 & §2.3 + non uniform beam §2.5 + Multi-beams code §2.7 + structural damping (Kelvin-Voigt damping) §2.5 + zero length interval §2.8 + aerodynamic damping (added mass term, Theodorsen) [16] + punctual mass loads §2.6 + arbitrary location of the tension, elastic and center of gravity axis §2.5 §2.6 + coupled to a non linear unsteady lifting line model [16]
continuous solution	discrete solution	discrete solution §2.8

Table 1: Evolution of the classical Euler-Bernoulli beam theory to the ASWING structural model.
References to the sections are displayed where the improvements are detailed

The c-axis is aligned with the chord line pointing downstream, the s-axis is tangent to the reference line and the n-axis is constructed using the right hand rule. As for the body frame, the local axes are rotated from the body axis according to the sequence shown in figure 3. The transformation matrix is given by

$$[T] = \begin{bmatrix} \cos \vartheta & 0 & -\sin \vartheta \\ 0 & 1 & 0 \\ \sin \vartheta & 0 & \cos \vartheta \end{bmatrix} \begin{bmatrix} \cos \psi & \sin \psi & 0 \\ -\sin \psi & \cos \psi & 0 \\ 0 & 0 & 1 \end{bmatrix} \begin{bmatrix} 1 & 0 & 0 \\ 0 & \cos \varphi & \sin \varphi \\ 0 & -\sin \varphi & \cos \varphi \end{bmatrix} \quad (6)$$

where $\vec{\theta} = (\varphi \ \vartheta \ \psi)^T$ are the local frame rotation angles. The latter vary with the reference line coordinate s . The position of the local frame origin is given by $\vec{r}(s)$ expressed in the body frame. In the unsteady formulation of the structural model, the local frame may have a relative velocity and orientation rate expressed in the body frame, denoted by $\vec{u}(s)$ and $\vec{\omega}$. The position and velocity $\vec{r}(s)$ and $\vec{u}(s)$ are related as follows

$$\vec{u}(s) = \frac{d\vec{r}(s)}{dt} \quad (7)$$

Relation between $\vec{\omega}$ and $\dot{\vec{\theta}}$ is not as trivial. Indeed $\vec{\theta}$ defines the rotation rate around x , s and z_1 . The last 2 are not part of the body frame. When x , y , z components of $\vec{\omega}$ are projected against \vec{x} , \vec{s} and \vec{z}_1 it comes :

$$\dot{\vec{\theta}} = [C]\vec{\omega} = \begin{bmatrix} 1 & \cos \varphi \tan \psi & \sin \varphi \tan \psi \\ 0 & \cos \varphi / \cos \psi & \sin \varphi / \cos \psi \\ 0 & -\sin \varphi & \cos \varphi \end{bmatrix} \begin{pmatrix} \omega_x \\ \omega_y \\ \omega_z \end{pmatrix} \quad (8)$$

where $[C]$ is the \vec{x} , \vec{y} and \vec{z} to \vec{x} , \vec{s} and \vec{z}_1 projection matrix. As it will be seen in the next section, $\vec{\omega}$ is more convenient than $\dot{\vec{\theta}}$ to derive the inertial acceleration of any point attached to the local frame.

2.2 Inertial acceleration

In order to calculate the inertial and gravitational loads derived in the following sections, the absolute acceleration¹ of a point rigidly attached to the local frame origin is required. To do this, an acceleration composition is used. First, the absolute acceleration of the local frame origin is given below. Terms of

interest are indicated by brackets.

$$\vec{a}(\vec{r}) = \vec{a}_o + \underbrace{\dot{\vec{u}}}_{\text{Coriolis}} + \underbrace{\vec{\alpha}_o \times \vec{r}}_{\text{swinging acceleration}} + \underbrace{\vec{\Omega} \times (\vec{\Omega} \times \vec{r})}_{\text{centrifugal acceleration}} + \underbrace{2\vec{\Omega} \times \vec{u}}_{\text{Coriolis}} \quad (9)$$

The blue terms in the equation in 9 highlight the unsteady terms. From the previous equation one can derive the absolute acceleration of any point "rigidly" connected to the csn frame by a pylon. By denoting \vec{r}_p the position of the point so that

$$\vec{r}_p = \vec{r}(s) + \delta \vec{r}_p = \vec{r}(s) + \begin{pmatrix} c_p \\ s_p \\ n_p \end{pmatrix}_{c,s,n}$$

Considering that (c, s, n) has a relative² rotation rate $\vec{\omega}$, the relative³ change of the offset vector is due only to this rotation and is given by

$$\vec{u}_p = \frac{d}{dt} \Delta \vec{r}_p = \vec{\omega} \times \Delta \vec{r}_p$$

Finally, the absolute acceleration of point p is

$$\vec{a}(\vec{r}_p) = \vec{a}_p = \vec{a}(\vec{r}) + \left(\vec{\alpha}_o + \dot{\vec{\omega}} \right) \times \Delta \vec{r}_p + \vec{\Omega} \times (\vec{\Omega} \times \Delta \vec{r}_p) + \vec{\omega}_i \times (\vec{\omega} \times \Delta \vec{r}_p) + 2\vec{\Omega} \times (\vec{\omega} \times \Delta \vec{r}_p) \quad (10)$$

2.3 Beam curvatures and strains

As will be explained in more detail in the next section, when any load (distributed or point) is applied to a beam, it experiences a change in its geometry. In this section, curvature and strains are introduced as they will be used to calculate internal forces and moments.

Curvature

When the local frame is moved along the reference line from a spanwise location s to $s + ds$, the (c, s, n) axes undergo a small rotation. Figure 4 shows a simplified case. The s and n axes undergo a small rotation of an angle $d\theta$ around the c axis. The latter angle is related to the curvature κ_c as follows: $d\theta = \kappa_c ds$. Note that $\frac{1}{\kappa_c}$ can be interpreted as the radius of curvature of the beam at the spanwise point s . A circle with its centre at the intersection of $n(s)$ and $n(s+ds)$ with the latter radius of curvature is perfectly tangent to the vectors $s(s)$ and $s(s+ds)$. Figure 4 shows the 2D case. In the 3D case the illustration is not so simple. As a result, when the local frame is moved along the reference line,

¹The absolute acceleration denotes the acceleration relative to the inertial frame.

²relative to the body frame

³relative to the csn frame

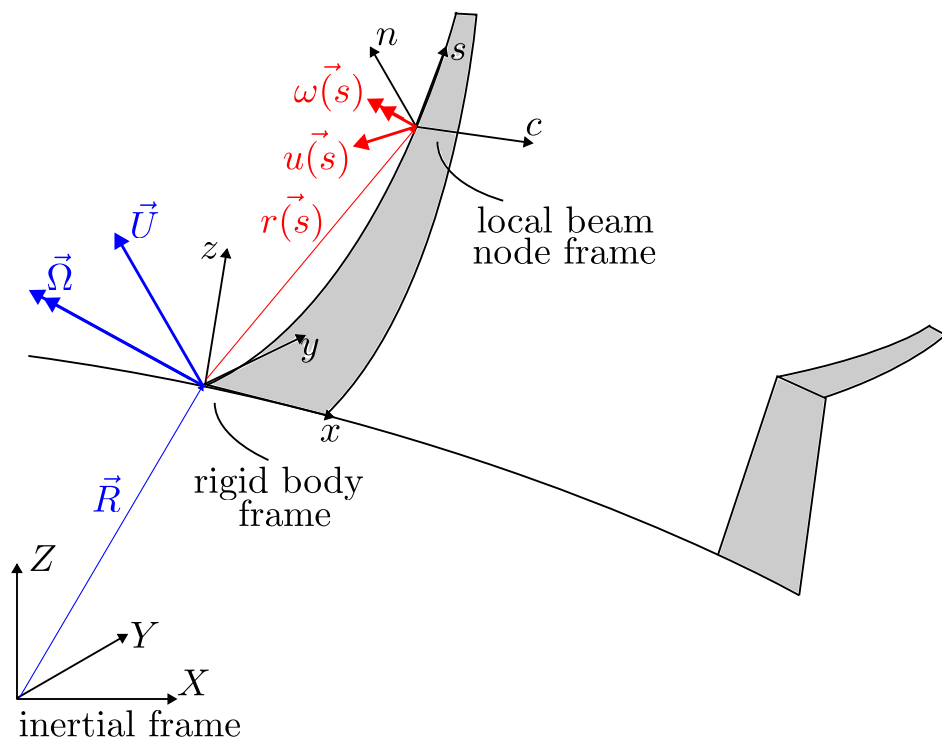


Figure 1: Structural model useful frames

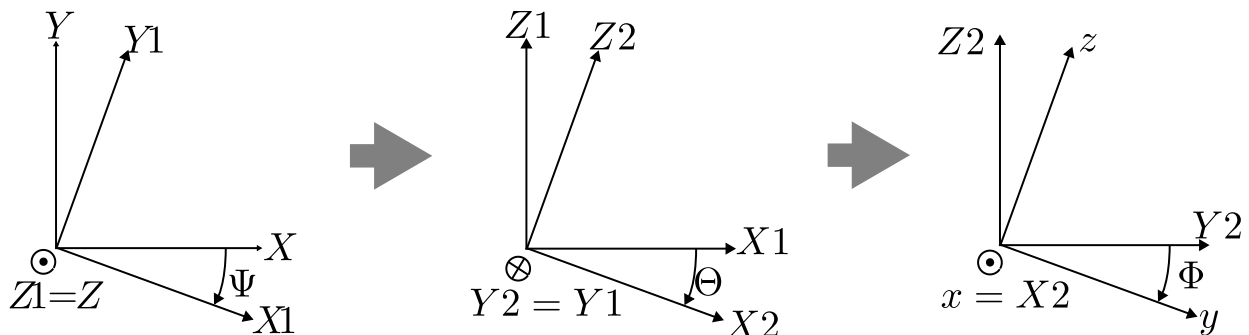


Figure 2: Earth to body frame transformation sequence

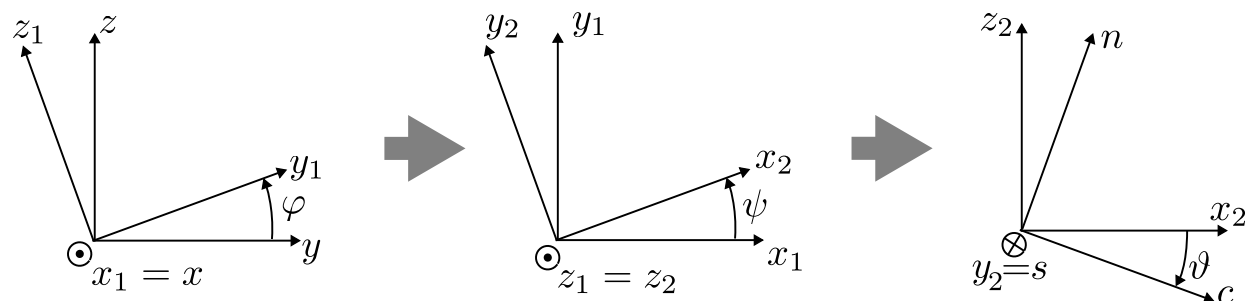


Figure 3: Body to local frame transformation sequence

it can undergo a small rotation as follows:

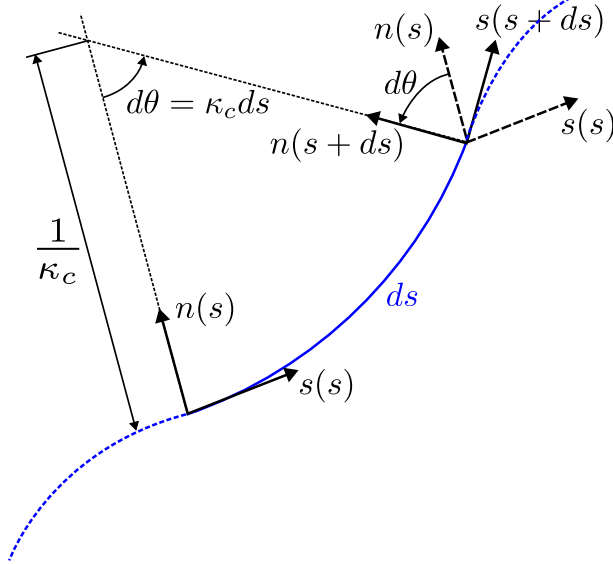


Figure 4: Beam local curvature, simplified case for illustration

$$\begin{aligned} \begin{pmatrix} c(s) \\ s(s) \\ n(s) \end{pmatrix} &= [T(s)] \begin{pmatrix} x \\ y \\ z \end{pmatrix} \\ \begin{pmatrix} c(s+ds) \\ s(s+ds) \\ n(s+ds) \end{pmatrix} &= \left[T(s) + \frac{d[T]}{ds} ds \right] \begin{pmatrix} x \\ y \\ z \end{pmatrix} \end{aligned} \quad (11)$$

The small elementary transformation in equation 11 is linked to the curvature as follow :

$$\frac{d[T]}{ds} = -[\mathcal{K}][T] = \begin{pmatrix} 0 & -\kappa_n & \kappa_s \\ \kappa_n & 0 & -\kappa_c \\ -\kappa_s & \kappa_c & 0 \end{pmatrix} [T(s)] \quad (12)$$

where $[\mathcal{K}]$ is the local curvature tensor. Using a mix of the scalar and vectorial product, the curvature c, s, n component can be obtained from equation 12 as follow:

$$\begin{aligned} \begin{pmatrix} \kappa_c \\ \kappa_s \\ \kappa_n \end{pmatrix} &= \begin{bmatrix} \cos \psi \cos \vartheta & 0 & -\sin \vartheta \\ -\sin \psi & 1 & 0 \\ \cos \psi \sin \vartheta & 0 & \cos \vartheta \end{bmatrix} \begin{pmatrix} d\varphi/ds \\ d\vartheta/ds \\ d\psi/ds \end{pmatrix} \\ &= [K] \begin{pmatrix} d\varphi/ds \\ d\vartheta/ds \\ d\psi/ds \end{pmatrix} \end{aligned} \quad (13)$$

where $[K]$ is the curvature definition matrix. Two types of beam curvature are of interest in the next sections, the loaded and the unloaded, denoted as $(\kappa_c, \kappa_s, \kappa_n)$ and $(\kappa_{c,0}, \kappa_{s,0}, \kappa_{n,0})$. The latter is ob-

tained with the equation 13 and is given as

$$\begin{pmatrix} \kappa_{c,0} \\ \kappa_{s,0} \\ \kappa_{n,0} \end{pmatrix} = [K_0] \begin{pmatrix} d\varphi_0/ds \\ d\vartheta_0/ds \\ d\psi_0/ds \end{pmatrix} \quad (14)$$

where $[K_0]$ is the unloaded curvature definition matrix. The unloaded curvature is of particular interest for modelling non-flat beams. Another quantity of interest to derive the internal forces and moments is the rate of curvature. The latter is given by deriving the equation 13 with respect to time. From now on the notations $\vec{\theta} = (\varphi, \vartheta, \psi)^T$ and $\vec{\theta}_0 = (\varphi_0, \vartheta_0, \psi_0)^T$ are used.

$$\begin{pmatrix} \dot{\kappa}_c \\ \dot{\kappa}_s \\ \dot{\kappa}_n \end{pmatrix} = [K] \frac{d\vec{\theta}}{ds} + [\dot{K}] \frac{d\vec{\theta}}{ds} \quad (15)$$

with $[\dot{K}]$ is given as follow

$$\begin{aligned} \dot{K} &= \frac{\partial[K]}{\partial\varphi} \dot{\varphi} + \frac{\partial[K]}{\partial\vartheta} \dot{\vartheta} + \frac{\partial[K]}{\partial\psi} \dot{\psi} \\ &= [K]_\varphi \dot{\varphi} + [K]_\vartheta \dot{\vartheta} + [K]_\psi \dot{\psi} \end{aligned}$$

Multiplying by $\frac{d\vec{\theta}}{ds}$ it comes:

$$\begin{aligned} [\dot{K}] \frac{d\vec{\theta}}{ds} &= ([K]_\varphi \dot{\varphi} + [K]_\vartheta \dot{\vartheta} + [K]_\psi \dot{\psi}) \frac{d\vec{\theta}}{ds} \\ &= \frac{d[K]}{ds} \vec{\theta} \end{aligned}$$

Using it in the equation 16 gives the final expression of the curvature rate

$$\begin{pmatrix} \dot{\kappa}_c \\ \dot{\kappa}_s \\ \dot{\kappa}_n \end{pmatrix} = [K] \frac{d\vec{\theta}}{ds} + \frac{d[K]}{ds} \vec{\theta} \quad (16)$$

Tension and shear strains: As explained earlier, the curvature provides information about how the local frame axes are rotated. Another useful piece of information is the displacement of the frame origin along the reference line. When the beam is unloaded, the position of the local frame at the spanwise location $s + ds$ is given by

$$\begin{aligned} \vec{r}(s+ds) &= \vec{r}(s) + [T(s)]^T ds_0 \begin{pmatrix} 0 \\ 1 \\ 0 \end{pmatrix}_{c,s,n} \\ &= \vec{r}(s) + \frac{d\vec{r}}{ds} ds \end{aligned} \quad (17)$$

where $d_{s,0}$ denotes the unloaded element length. Now, supposing that the beam is locally subject to shear and extensional stress, the csn origin is shifted as

follows

$$\begin{aligned}\vec{r}(s+ds) &= \vec{r}(s) + [T(s)]^T ds_0 \begin{pmatrix} \gamma_c \\ \epsilon_s + 1 \\ \gamma_n \end{pmatrix}_{c,s,n} \quad (18) \\ &= \vec{r}(s) + \frac{d\vec{r}}{ds} ds\end{aligned}$$

The difference between the loaded and unloaded csn origin shift is shown in the figure 5. It is important to note that the strains have no dimensions, the shift induced by them is proportional to ds . The equation 18 can be inverted to obtain the relation between the strains and the variation of the local position vector with respect to the spanwise location.

$$\begin{pmatrix} \gamma_c \\ \epsilon_s + 1 \\ \gamma_n \end{pmatrix}_{c,s,n} = [T(s)] \frac{d\vec{r}}{ds_0} \quad (19)$$

As for the curvature, the strain rates will be useful. Deriving equation 19 with respect to time leads to

$$\begin{pmatrix} \dot{\gamma}_c \\ \dot{\epsilon}_s \\ \dot{\gamma}_n \end{pmatrix}_{c,s,n} = [T(s)] \frac{d\vec{r}}{ds_0} + [\dot{T}(s)] \frac{d\vec{r}}{ds_0} \quad (20)$$

The transformation matrix rate $[\dot{T}(s)]$ is actually related to $\vec{\omega}(s)$ with $[\dot{T}(s)] = -T(s)[\omega(s)]$ ⁴. Based on that the stains rates are related to the local frame origin speed, position and rotation rates as follows

$$\begin{pmatrix} \dot{\gamma}_c \\ \dot{\epsilon}_s \\ \dot{\gamma}_n \end{pmatrix}_{c,s,n} = [T(s)] \left(\frac{d\vec{u}}{ds_0} - \vec{\omega}(s) \times \frac{d\vec{r}}{ds_0} \right) \quad (21)$$

2.4 Forces and moment equilibrium

Let us consider a beam element of length ds , (cf figure 6). Applying the Newton's principle comes :

$$\begin{aligned}-F(\vec{s}) + \vec{F}(s+ds) + \vec{f}ds + \Delta\vec{F}\delta(1) &= 0 \\ d\vec{F}(s) + \vec{f}ds + \Delta\vec{F}\delta(1) &= 0\end{aligned} \quad (22)$$

where $F(\vec{s})$ denotes the internal beam force, \vec{f} are the distributed forces (lift and drag) and $\Delta\vec{F}$ the point loads (engine, struts, point mass, joints). In this report only the point mass and the distributed inertia and gravity loads are derived, as they will be derived later. The others (lift, drag, engine) are described in [16, 17]. The moment equilibrium around the left

element is given by :

$$\begin{aligned}-M(\vec{s}) + \vec{M}(s+ds) + \vec{m}ds + \Delta\vec{M}\delta(1) \\ + [T]^T \begin{pmatrix} 0 \\ ds \\ 0 \end{pmatrix}_l \times \vec{F}(s+ds) &= 0 \\ d\vec{M}(s) + \vec{m}ds + \Delta\vec{M}\delta(1) \\ + [T]^T \begin{pmatrix} 0 \\ ds \\ 0 \end{pmatrix}_l \times \vec{F}(s+ds) &= 0\end{aligned} \quad (23)$$

Note that the moments induced by the distributed loads f are already included in the distributed moments m .

2.5 Internal forces and moments in non uniform beams

From the expressions of strain and curvature expressed in the local frame (c, s, n) , the internal forces can be derived. In fact, the shear and extensional strains and the bending/torsional curvature provide information on how the length of the fibres changes in the beam element. Firstly, ASWING differs from the classical Euler-Bernoulli or its non-linear extension (Minguet) in that it takes into account the stiffness properties of non-uniform sections. Figure 7 shows what motivated this change. Wings are made of different materials, the shell can be made of carbon fibre with specific tailoring, balsa, aluminium foam, etc. The main and secondary spars can be made of plywood, aluminium, plywood covered with carbon fibre, etc. The latter have different Young's and Coulomb's moduli. Consequently, in the next development the E and G moduli will be considered as varying with the section coordinates (c, n) . The next development will be divided into different parts where each strain and curvature contribution to forces and moments will be considered.

Forces and moments due to extensional strains:

Assuming that the section does not wrap, the extensional strain $\epsilon_s(s)$ does not vary in the section plane (c, n) and is considered to be uniform. When a beam element fibre is stretched to length $ds + \epsilon(s)ds$, the elementary extensional force due to $\epsilon_s(s)$ is given by

$$d\vec{f}_{\epsilon_s} = E(c, n)\epsilon_s dcdn \vec{s}$$

where $dcdn$ is a small cross-sectional element area. Since the beam element Young's modulus E is not uniform along the section, the extensional stress is also not uniform as shown in the figure 8. Since a wing section does not have the shape of a plate, the strain stress is not uniform, but also does not occur along the entire chord depending on the section

⁴ $[\omega(s)]$ must not be confused with $\vec{\omega}(s)$, $[\omega(s)]$ is the rotation rate tensor

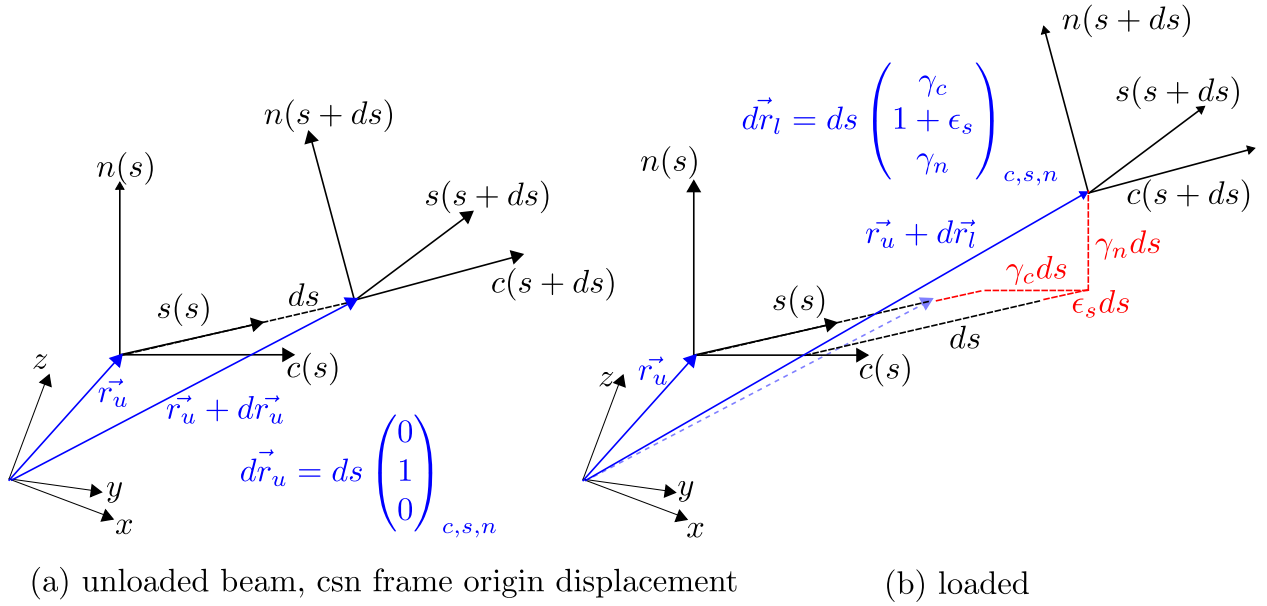


Figure 5: extensional and shear strains illustration

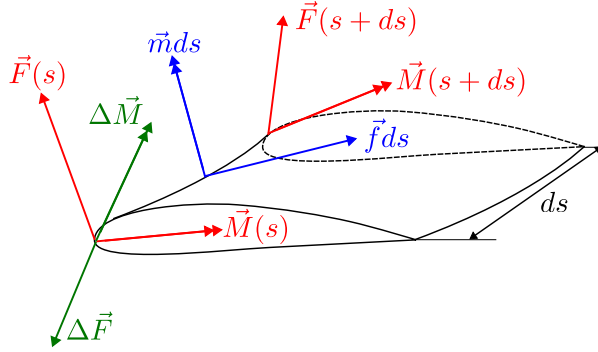


Figure 6: Forces and moments equilibrium on a beam element

layer considered, as shown on the right side of the figure. This non-uniformity leads to the lumping of the extensional stress around the tension axis of the coordinate (c_{TA} , n_{TA}). The latter is not necessarily at the centre of the chord and half the thickness as in classical Euler-Bernoulli theory. Overall, the internal stress due to an extensional strain is given by integrating the elementary stress over the section

$$F_{s,\epsilon_s} = \epsilon_s \iint E(c, n) \vec{s} dcdn = EA\epsilon_s \quad (24)$$

EA must not be confused with the Young modulus E multiplied by the cross-section area. Another proposition of this model is to add structural damping and assume the extensional stress varies proportionally with the strain rate as follows

$$F_{s,\epsilon_s} = \epsilon_s \iint E(c, n) \vec{s} dcdn = EA(\epsilon_s + t_e \dot{\epsilon}_s) \quad (25)$$

where t_e is the extensional damping time. The added term (in blue) is known as the Kelvin-Voigt damping factor (Banks and Wang 1987, 1991). Also EA must not be confused with the Young modulus E multiplied by the cross-section area A . As highlighted above, another proposition of this model is to add structural damping and assume the extensional stress varies proportionally with the strain rate. For the sake of clarity, the latter expression will be considered in its steady state form for the next development. The unsteady terms will be reintroduced in the final strain/curvature force/moment relations. From the above equation, the position of the tension axis (tension barycentre) can be derived as follows

$$\begin{aligned} c_{TA} &= \frac{\iint cE(c, n) \vec{s} dcdn}{\iint E(c, n) \vec{s} dcdn} = \frac{\iint cE(c, n) \vec{s} dcdn}{EA} \\ n_{TA} &= \frac{\iint nE(c, n) \vec{s} dcdn}{EA} \end{aligned} \quad (26)$$

From equations 25 and 26, the moments due to F_{s,ϵ_s} at the c, s, n origin can be given as:

$$\begin{aligned} \begin{pmatrix} M_{c,\epsilon_s} \\ 0 \\ M_{n,\epsilon_s} \end{pmatrix} &= \begin{pmatrix} M_{c',\epsilon_s} \\ 0 \\ M_{n',\epsilon_s} \end{pmatrix} + \begin{pmatrix} c_{TA} \\ 0 \\ n_{TA} \end{pmatrix} \times \begin{pmatrix} 0 \\ F_{s,\epsilon_s} \\ 0 \end{pmatrix} \\ \begin{pmatrix} M_{c,\epsilon_s} \\ 0 \\ M_{n,\epsilon_s} \end{pmatrix} &= \begin{bmatrix} 0 & -n_{TA} & 0 \\ 0 & 0 & 0 \\ 0 & c_{TA} & 0 \end{bmatrix} \begin{pmatrix} \gamma_c \\ \epsilon_s \\ \gamma_n \end{pmatrix} \end{aligned} \quad (27)$$

where c' and n' are vectors associated with the stress axis as shown in the figure 8.

Forces and moments due to c and n shear strains:

The same analysis as above is not possible for c and n shear stresses. The shear stiffness of the section is

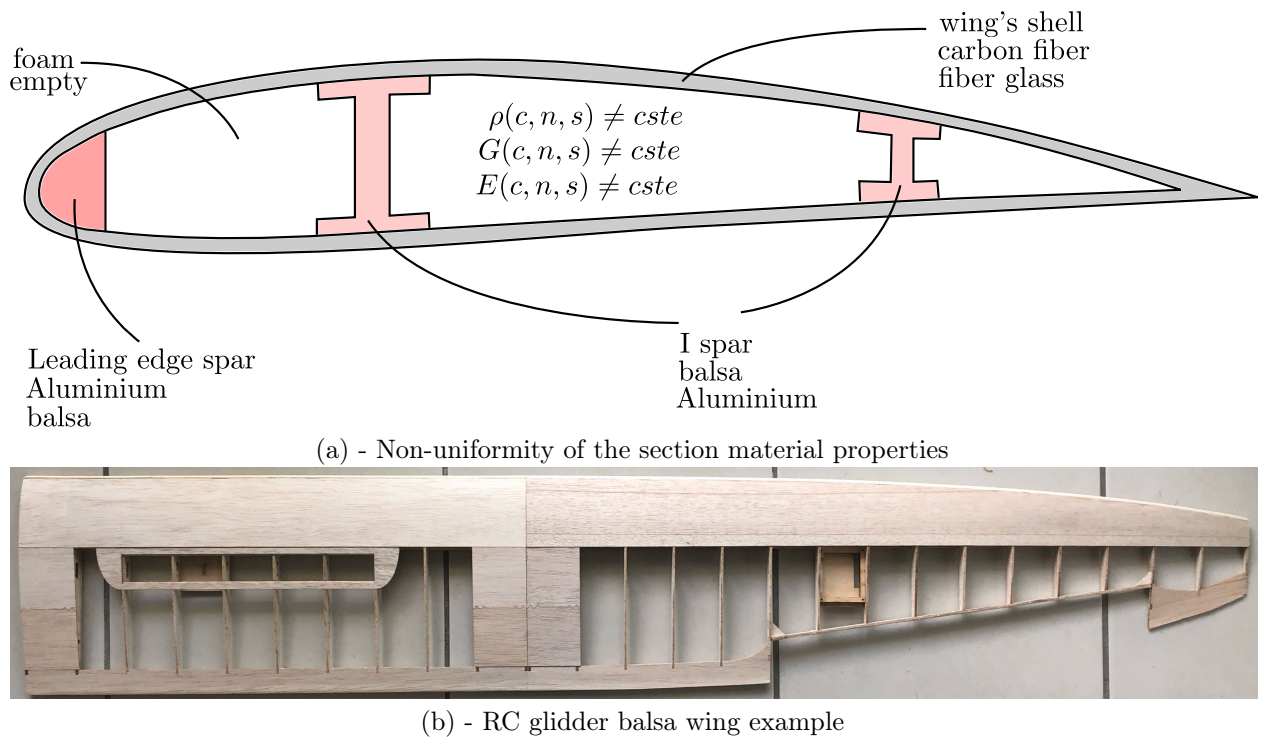


Figure 7: Non-uniformity of the section material properties

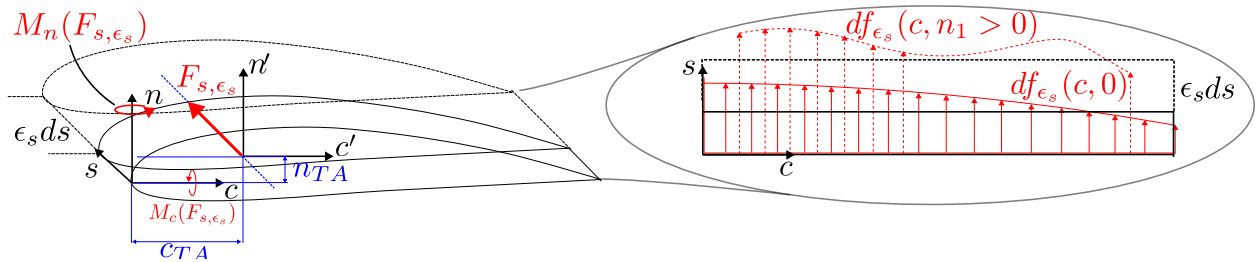


Figure 8: Non uniform extensional load distribution, lumping on the tension axis

still considered non-uniform and so are the induced shear stresses. The c -shear stresses can be grouped on a horizontal elastic line with an offset from the c -axis marked n_{EA} as shown in figure 9. In the same way the n -shear stresses are lumped on a vertical elastic line having an offset with the n -axis noted as c_{EA} . The intersection of the elastic lines defines the elastic axis of the section. The c and n -shear stresses are given as below

$$\begin{pmatrix} F_{c,\gamma} \\ F_{s,\gamma} \\ F_{n,\gamma} \end{pmatrix} = \begin{bmatrix} GK_c & 0 & 0 \\ 0 & 0 & 0 \\ 0 & 0 & GK_n \end{bmatrix} \begin{pmatrix} \gamma_c \\ 0 \\ \gamma_n \end{pmatrix} \quad (28)$$

where GK_c and GK_n are the c and n shear stiffnesses respectively. Note that neither the shear stiffness nor the elastic axis coordinate (c_{EA}, n_{EA}) integral expressions (such as Eq 25 and 26) exist. They can be obtained using shear flow analysis codes such as Co-Blade. As for the extensional stress, the shear stress is also assumed to vary proportionally to the shear strain rate. The unsteady terms will be recalled later and are avoided for now. Note that the zero off-diagonal terms in the equations 29 emphasise the hypothesis that there are no cross-coupling terms between stresses and strains. In practice, this is not a conservative assumption, as bending stiffnesses are mostly dominant in wings. Nevertheless, the moments at the csn frame origin due to c and n strains are given by :

$$\begin{pmatrix} F_{c,\gamma} \\ F_{s,\gamma} \\ F_{n,\gamma} \end{pmatrix} = \begin{bmatrix} GK_c & 0 & 0 \\ 0 & 0 & 0 \\ 0 & 0 & GK_n \end{bmatrix} \begin{pmatrix} \gamma_c + t_\gamma \dot{\gamma}_c \\ 0 \\ \gamma_n + t_\gamma \dot{\gamma}_n \end{pmatrix} \quad (29)$$

The unsteady terms will be recalled later and are avoided for now. Note that the zero off-diagonal terms in the equations 28 emphasise the hypothesis that there are no cross-coupling terms between stresses and strains. In practice, this is not a conservative assumption, as bending stiffnesses are mostly dominant in wings. Nevertheless, the moments at the csn frame origin due to c and n strains are given by :

$$\begin{pmatrix} M_{c,\gamma} \\ M_{s,\gamma} \\ M_{n,\gamma} \end{pmatrix} = \begin{pmatrix} 0 \\ M_{s',\gamma} \\ 0 \end{pmatrix} + \begin{pmatrix} c_{EA} \\ 0 \\ n_{EA} \end{pmatrix} \times \begin{pmatrix} F_{c,\gamma} \\ 0 \\ F_{n,\gamma} \end{pmatrix} \quad (30)$$

$$\begin{pmatrix} 0 \\ M_{s,\gamma} \\ 0 \end{pmatrix} = \begin{bmatrix} 0 & 0 & 0 \\ n_{EA} & 0 & -c_{EA} \\ 0 & 0 & 0 \end{bmatrix} \begin{pmatrix} \gamma_c \\ \epsilon_s \\ \gamma_n \end{pmatrix}$$

The forces and moments due to shear and extensional strains remain those due to bending and torsional curvatures.

Forces and moments due to c and n curvatures: Before deriving the force and moment expressions, another proposed feature must be highlighted. The ASWING structural model can consider a non-

flat/straight beam. Geometrically, this means that the unloaded beam can have a non-zero curvature. Figure 10 (a) and (b) shows the previous idea and compares it with the classical non-linear Euler-Bernoulli theory. It is said that when a beam is bent or twisted it experiences a change in its curvature. This causes a change in the length of the fibre. For example, in figure 10 (b), the inner side of the elements sees its fibres "contracted" and the outer side "extended". These notions of extension/contraction are relative to the way the user has defined the elementary unloaded length ds . This can be seen in the figure 10 (a) where the element ds has been defined at the leading edge of the wing, whereas in classical theory it was defined at the mid-chord. This has no effect on the loads and moments. The position of the local frame can be arbitrary as long as it is in the cross section. As mentioned above, a change in curvature induces a local change in fibre length, i.e. strain. The latter is therefore not uniform across the section. The induced strain is calculated relative to the element length ds . In the ASWING structural model it is calculated relative to the unloaded curvature. Only the case for the n -curvature is derived, as the other one follows the same principle. The local strain induced by the n -curvature is given by

$$\begin{aligned} \epsilon_{s,\kappa_n}(c) &= \frac{\left(\frac{1}{\kappa_n}d\theta + c\right) - \left(\frac{1}{\kappa_{n,0}}d\theta_0 + c\right)}{\frac{1}{\kappa_{n,0}}d\theta_0} \\ &= c(\kappa_n - \kappa_{n,0}) \end{aligned} \quad (31)$$

with $\left(\frac{1}{\kappa_n}d\theta + c\right)$ and $\left(\frac{1}{\kappa_{n,0}}d\theta_0 + c\right)$ denotes the loaded and unloaded arc length at the chordwise location c (cf figure 10-a). In the same way the extensional strain due to the c -curvature is given by

$$\epsilon_{s,\kappa_c} = -n(\kappa_c - \kappa_{c,0}) \quad (32)$$

where the minus sign is related to the axis definition. From the induced strain the local extension stress is given as:

$$df_{s,\kappa} = E(c, s) (c(\kappa_n - \kappa_{n,0}) - n(\kappa_c - \kappa_{c,0})) dc dn$$

The above expression highlights a peculiarity of a non-uniform beam. As the Young's modulus varies across the section, this will result in a asymmetric load distribution about the mid chord, as it should be in classical Euler-Bernoulli theory. This is highlighted in figure 11-(b). Because of the asymmetry property, the extensional loads cancel each other out but produce a bending moment. If the Young's modulus is not uniform, a non-zero extension load is possible (see figure 11-a). This is emphasised by the following integration of the elementary extension loads over the section

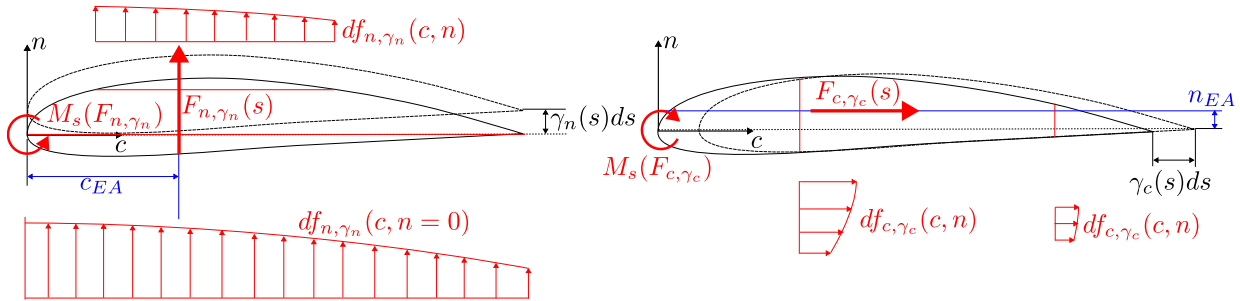


Figure 9: Non uniform c and n shear loads due to c and n strains. Lumping on the c-shear and s-shear elastic lines

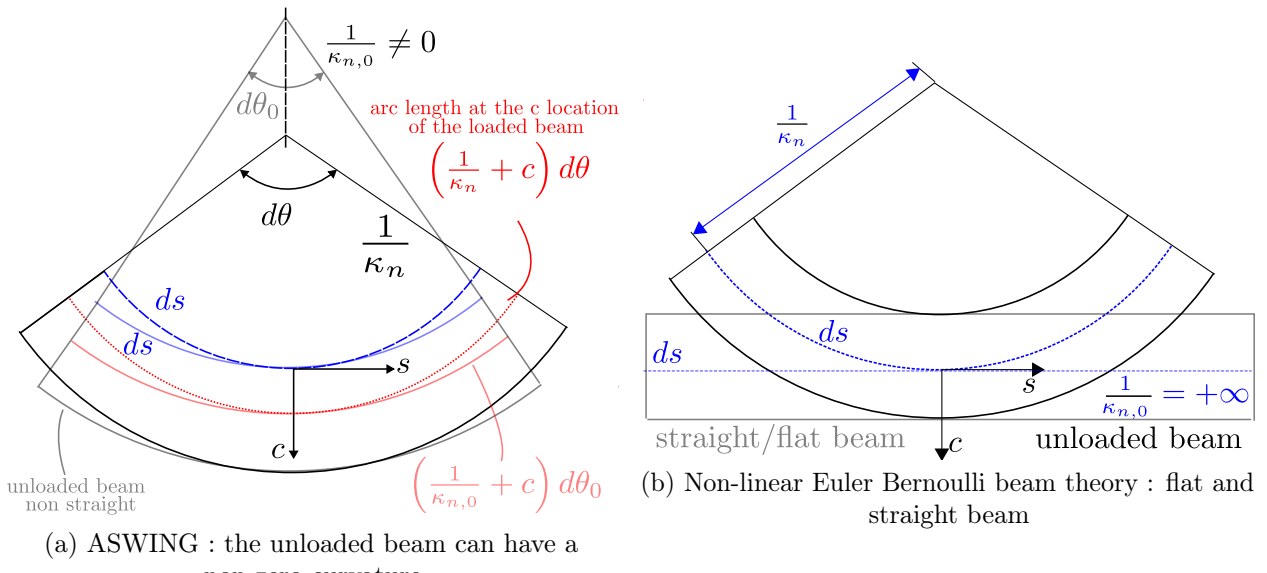


Figure 10: ASWING vs classical Euler-Bernoulli beam theory: zero curvature

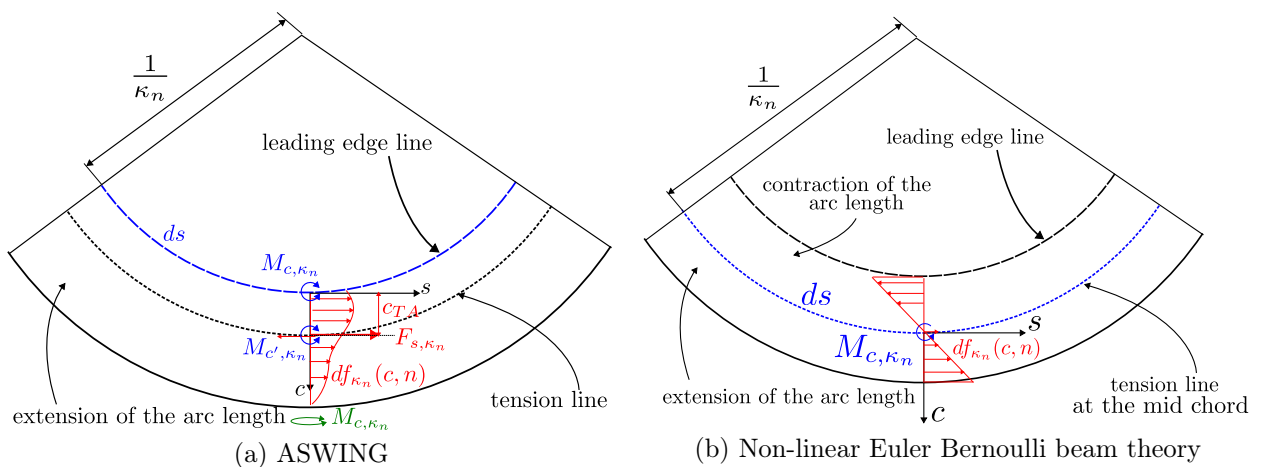


Figure 11: ASWING vs classical Euler Bernoulli beam theory: loads distribution

$$F_{s,\kappa} = \iint E(c, s) (c(\kappa_n - \kappa_{n,0}) - n(\kappa_c - \kappa_{c,0})) dcdn$$

The curvature being uniform across the section the above equation is rewritten

$$F_{s,\kappa} = (\kappa_n - \kappa_{n,0}) \iint cE(c, s) dcdn - (\kappa_c - \kappa_{c,0}) \iint nE(c, s) dcdn$$

The first and second terms can be rewritten identifying the tension axis chordwise and normal coordinate.

$$F_{s,\kappa} = (\kappa_n - \kappa_{n,0}) c_{TA} EA - n_{TA} (\kappa_c - \kappa_{c,0}) EA$$

$$\begin{pmatrix} F_{s,\kappa} \\ 0 \end{pmatrix} = \begin{bmatrix} 0 & 0 & 0 \\ -n_{TA} EA & 0 & c_{TA} EA \\ 0 & 0 & 0 \end{bmatrix} \begin{pmatrix} \kappa_c - \kappa_{c,0} + t_{\epsilon} \dot{\kappa}_c \\ 0 \\ \kappa_n - \kappa_{n,0} + t_{\epsilon} \dot{\kappa}_n \end{pmatrix} \quad (33)$$

In the same way the torsion (s -curvature) change induces a non-uniform c and n shear stress load distribution, when integrated across the section the loads induced are given as

$$\begin{pmatrix} F_{c,\kappa_s} \\ 0 \\ F_{n,\kappa_s} \end{pmatrix} = \begin{bmatrix} 0 & GK_c n_{EA} & 0 \\ 0 & 0 & 0 \\ 0 & -GK_n c_{EA} & 0 \end{bmatrix} \begin{pmatrix} 0 \\ \kappa_s - \kappa_{s,0} + t_{\gamma} \dot{\kappa}_s \\ 0 \end{pmatrix} \quad (34)$$

As for the strain loads, the unsteady structural damping terms have been added to the above equations. From equations 25, 29, 33 and 34 the final form of

the load strain/curvature relation is given

$$\begin{pmatrix} F_c \\ F_s \\ F_n \end{pmatrix} = \begin{bmatrix} GK_c & 0 & 0 \\ 0 & EA & 0 \\ 0 & 0 & GK_n \end{bmatrix} \begin{pmatrix} 0 & GK_c n_{EA} & 0 \\ -EAn_{EA} & 0 & EA c_{EA} \\ 0 & -GK_n c_{EA} & 0 \end{pmatrix} \begin{pmatrix} \gamma_c + t_{\gamma} \dot{\gamma}_c \\ \epsilon_s + t_{\epsilon} \dot{\epsilon}_s \\ \gamma_n + t_{\gamma} \dot{\gamma}_n \\ \kappa_c - \kappa_{c,0} + t_{\epsilon} \dot{\kappa}_c \\ \kappa_s - \kappa_{s,0} + t_{\gamma} \dot{\kappa}_s \\ \kappa_n - \kappa_{n,0} + t_{\epsilon} \dot{\kappa}_n \end{pmatrix} \quad (35)$$

$$= [\mathcal{E}_{F,\gamma} \quad \mathcal{E}_{F,\kappa}] \begin{pmatrix} \gamma_c + t_{\gamma} \dot{\gamma}_c \\ \epsilon_s + t_{\epsilon} \dot{\epsilon}_s \\ \gamma_n + t_{\gamma} \dot{\gamma}_n \\ \kappa_c - \kappa_{c,0} + t_{\epsilon} \dot{\kappa}_c \\ \kappa_s - \kappa_{s,0} + t_{\gamma} \dot{\kappa}_s \\ \kappa_n - \kappa_{n,0} + t_{\epsilon} \dot{\kappa}_n \end{pmatrix}$$

where $[\mathcal{E}_{F,\gamma}]$ and $[\mathcal{E}_{F,\kappa}]$ are the load/strain and load/curvature stiffness matrices respectively which parameters can be identified from the previous development. The moments induced by a change in curvature must be derived. It is interesting to note that the load induced by the c and n shear strains does not induce a moment about s' because of the uniformity of the strains. The same observation is made for the load induced by the extensional strain, but for the c' and n' axes. The moments about these axes are then derived. A change in the s -curvature induces unevenly distributed c and n loads, the moments due to the latter are then given along each axis as follows

$$\begin{pmatrix} M_{c',\kappa_s} \\ M_{s',\kappa_s} \\ M_{n',\kappa_s} \end{pmatrix} = \begin{bmatrix} 0 & E_{cs} & 0 \\ E_{cs} & GJ & E_{sn} \\ 0 & E_{sn} & 0 \end{bmatrix} \begin{pmatrix} 0 \\ \kappa_s - \kappa_{s,0} + t_{\gamma} \dot{\kappa}_s \\ 0 \end{pmatrix} \quad (36)$$

where GJ is the torsional stiffness, E_{sn} and E_{cs} are the torsional bending coupling terms. Shear flow codes must be used to obtain their values⁵. In the case of aircraft, GJ and E_{cs} are of most interest. For the bending stiffness, real values can be derived. First of all, as the moments are calculated along c' , s' , a small change of variable is required. The elementary loads due to a change in curvature c and n are given by

$$df_{s,\kappa} = E(c, s) ((c - c_{TA})(\kappa_n - \kappa_{n,0}) - (n - n_{TA})(\kappa_c - \kappa_{c,0})) dcdn \quad (37)$$

⁵For shell wings, torsional stiffness formulae exist and are recalled in Drela (2008)

$GJ = 4GA_{sh}^2 t_{sh}/S_{sh}$ with A_{sh} , S_{sh} and t_{sh} being the enclosed area, perimeter and wall thickness of the shell respectively

where $(c - c_{TA})$ and $(n - n_{TA})$ are the distances relative to the tension axis. Note that the above equation implies that the element length ds must be defined along the tension axis to be consistent with previous developments. The elementary moments induced at c' and s' are then given as

$$\begin{aligned} dm_{s,\kappa} &= E(c,n) \begin{pmatrix} c - c_{TA} \\ 0 \\ n - n_{TA} \end{pmatrix} \times \begin{pmatrix} 0 \\ df_{s,\kappa} \\ 0 \end{pmatrix} dc dn \\ &= E(c,n) \begin{pmatrix} (n - n_{TA})^2 (\kappa_c - \kappa_{c,0}) \\ 0 \\ (n - n_{TA})(c - c_{TA})(\kappa_c - \kappa_{c,0}) \\ + (n - n_{TA})(c - c_{TA})(\kappa_n - \kappa_{n,0}) \\ 0 \\ +(c - c_{TA})^2 (\kappa_n - \kappa_{n,0}) \end{pmatrix} dc dn \end{aligned}$$

When integrated over the section comes the following matrix form

$$\begin{pmatrix} M_{c',\kappa_s} \\ M_{s',\kappa_s} \\ M_{n',\kappa_s} \end{pmatrix} = \begin{bmatrix} EI_{cc} & 0 & EI_{cn} \\ 0 & 0 & 0 \\ EI_{nc} & 0 & EI_{nn} \end{bmatrix} \begin{pmatrix} \kappa_c - \kappa_{c,0} + t_{\epsilon} \dot{\kappa}_c \\ 0 \\ \kappa_n - \kappa_{n,0} + t_{\epsilon} \dot{\kappa}_n \end{pmatrix}$$

with

$$\begin{aligned} EI_{cc} &= \iint E(c,s)(n - n_{TA})^2 dc dn \\ EI_{nn} &= \iint E(c,s)(c - c_{TA})^2 dc dn \\ EI_{cn} &= EI_{nc} \\ &= \iint E(c,s)(c - c_{TA})(n - n_{TA}) dc dn \end{aligned} \quad (38)$$

Combine to moment induced by the s curvature comes the final moment-curvature relation

$$\begin{aligned} \begin{pmatrix} M_{c'} \\ M_{s'} \\ M_{n'} \end{pmatrix} &= \begin{bmatrix} EI_{cc} & EI_{cs} & EI_{cn} \\ EI_{sc} & GJ & EI_{sn} \\ EI_{nc} & EI_{ns} & EI_{nn} \end{bmatrix} \begin{pmatrix} \kappa_c - \kappa_{c,0} + t_{\epsilon} \dot{\kappa}_c \\ \kappa_s - \kappa_{s,0} + t_{\gamma} \dot{\kappa}_s \\ \kappa_n - \kappa_{n,0} + t_{\epsilon} \dot{\kappa}_n \end{pmatrix} \\ &= [E(s)] \begin{pmatrix} \kappa_c - \kappa_{c,0} + t_{\epsilon} \dot{\kappa}_c \\ \kappa_s - \kappa_{s,0} + t_{\gamma} \dot{\kappa}_s \\ \kappa_n - \kappa_{n,0} + t_{\epsilon} \dot{\kappa}_n \end{pmatrix} \end{aligned} \quad (39)$$

The equation 39 is not consistent with the moment equilibrium equation 23 as the moments must be computed along the c,s,n axis. However, the latter has a very interesting feature in the sense that it can

be inverted as

$$\begin{pmatrix} \kappa_c - \kappa_{c,0} + t_{\epsilon} \dot{\kappa}_c \\ \kappa_s - \kappa_{s,0} + t_{\gamma} \dot{\kappa}_s \\ \kappa_n - \kappa_{n,0} + t_{\epsilon} \dot{\kappa}_n \end{pmatrix} = [E]^{-1} \begin{pmatrix} M_{c'} \\ M_{s'} \\ M_{n'} \end{pmatrix} \quad (40)$$

From the previous equation can be derived the strain/-moment relation

$$\begin{pmatrix} \gamma_c + t_{\gamma} \dot{\gamma}_c \\ \epsilon_s + t_{\epsilon} \dot{\epsilon}_s \\ \gamma_n + t_{\gamma} \dot{\gamma}_n \end{pmatrix} = [\mathcal{E}_{F,\gamma}]^{-1} \begin{pmatrix} F_c \\ F_s \\ F_n \end{pmatrix} - [\mathcal{E}_{F,\kappa}] [E]^{-1} \begin{pmatrix} M_{c'} \\ M_{s'} \\ M_{n'} \end{pmatrix} \quad (41)$$

The equations 40 and 41 are of particular interest as they allow the restriction of some of the beam degrees of freedom. Analytically it is equivalent to imposing coefficients of the stiffness matrices $[E]$ and $[\mathcal{E}_{F,\gamma}]$ to ∞ . However, this is not numerically possible if the equations 35 and 39 are implemented in this way. The inverse relationship is preferred because the coefficients of $[E]^{-1}$ and $[\mathcal{E}_{F,\gamma}]^{-1}$ can be set to zero to restrict the beam degrees of freedom. If some of the stiffness coefficients are unknown, they are automatically set to ∞ . This allows the user to completely ignore the structural dynamics if required. As a result, ASWING can also be used as a pure rigid aerodynamic pre-design tool if required.

2.6 Distributed/ponctual inertial and gravity loads

So far, the beam has been considered to be mass and inertial-less. However, each beam element in motion generates inertial loads and moments and is subject to gravity. A feature proposed by the ASWING structural model is to arbitrarily set the location of the sectional centre of gravity. In fact, the materials used to construct the wing may have different mass density for isoelastic properties (E,G) or vice versa. Consequently, the elastic, tensile and centre of gravity axes are not necessarily in the same place. Nevertheless, let us consider a concentrated mass/length that is lumped at the centre of mass location and rigidly attached to the local frame. The position relative to the csn frame (shown in figure 12) is given by

$$\Delta \vec{r}_{cg} = \begin{pmatrix} c_{cg} \\ 0 \\ n_{cg} \end{pmatrix}_l$$

The inertial loads of the lumped mass are given by its acceleration relative to the inertial (earth) frame. Summed to the gravity effect comes the inertial and

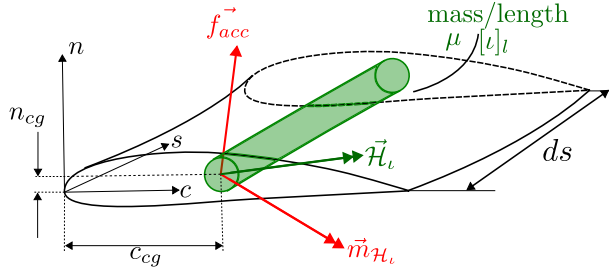


Figure 12: Distributed inertial and gravity loads, vector directions are arbitrary

gravity loads of the mass/length

$$\vec{f}_{acc} = \mu (\vec{g} - \vec{a}_{cg}) \quad (42)$$

with

$$\begin{aligned} \mu &= \iint \rho(c, s) dcdn, \\ c_{cg} &= \frac{\iint \rho(c, s) cdcdn}{\mu}, \\ n_{cg} &= \frac{\iint \rho(c, s) ndcdn}{\mu} \end{aligned}$$

where $\mu(s)$ is the local mass/length. The latter can vary along the span. \vec{a}_{cg} is computed using equation 9 with $\Delta \vec{r}_p = \Delta \vec{r}_{cg}$. The lumped mass is "concentrated" ie not punctual, in consequence, a local inertia/length tensor is introduced and denoted as $[\iota(s)]_l$. The mass/length can vary along the reference line and is expressed in the local frame as follow

$$[\iota]_l = \begin{bmatrix} \iota_{cc} & 0 & 0 \\ 0 & \iota_{ss} & 0 \\ 0 & 0 & \iota_{nn} \end{bmatrix} + \frac{ds^2}{12} \begin{bmatrix} \mu & 0 & 0 \\ 0 & 0 & 0 \\ 0 & 0 & \mu \end{bmatrix}_l$$

with

$$\begin{aligned} \iota_{cc} &= \iint \rho(c, s) (n - n_{cg})^2 dcdn, \\ \iota_{nn} &= \iint \rho(c, s) (c - c_{cg})^2 dcdn, \\ \iota_{ss} &= \iota_{cc} + \iota_{nn} \end{aligned}$$

This concentrated mass, being rigidly attached to the body frame, its rotation rate relative to the inertial frame is given by summing the relative rotation rate of the body and local frame $\vec{\Omega}$ and $\vec{\omega}$. The mass has in consequence an angular momentum because of its non-zero inertia tensor

$$\vec{\mathcal{H}}_{\iota,b} = [T]^T [\iota]_l [T] (\vec{\Omega} + \vec{\omega})_b$$

The transformation matrix $[T]$ and its inverse are used to express the rotation rate in the local frame as the inertia/length tensor. The inverse transformation $[T]^T$ is used to provide the angular momentum/length in the body frame. The torque induced by the angular momentum is given by its derivation with respect to

time

$$\begin{aligned} \vec{m}_{\mathcal{H}_t} &= - \frac{d ([T]^T [\iota]_l [T])}{dt} (\vec{\Omega} + \vec{\omega})_b \\ &\quad - [T]^T [\iota]_l [T] \frac{d (\vec{\Omega} + \vec{\omega})}{dt} \\ &= - \frac{d \vec{\mathcal{H}}_{\iota,b}}{dt} = - [T]^T [\iota]_l [T] (\vec{\alpha}_o + \vec{\dot{\omega}}) \\ &\quad - (\vec{\Omega} + \vec{\omega}) \times \underbrace{\{ [T]^T [\iota]_l [T] (\vec{\Omega} + \vec{\omega}) \}}_{\mathcal{H}_{\iota,b}} \end{aligned}$$

The distributed inertia and gravity moments about the csn origin are given by summing the angular momentum and the inertia/gravity loads moment as follows

$$\begin{aligned} \vec{m}_{acc} &= \Delta \vec{r}_{cg} \times \vec{f}_{acc} + \vec{m}_{\mathcal{H}_t} \\ \vec{m}_{acc} &= \Delta \vec{r}_{cg} \times \vec{f}_{acc} - [T]^T [\iota]_l [T] (\vec{\alpha}_o + \vec{\dot{\omega}}) \\ &\quad - (\vec{\Omega} + \vec{\omega}) \times \underbrace{\{ [T]^T [\iota]_l [T] (\vec{\Omega} + \vec{\omega}) \}}_{\mathcal{H}_{\iota,b}} \end{aligned} \quad (43)$$

Ponctual mass inertia and gravity loads

The second type of mass being considered in the model are punctual masses. They are used to reproduce the effect of a nacelle, sensors, actuators etc. They can generate 3 types of loads, engine thrust and torque, drag, inertia and gravity loads. Only the third and last one will be derived. First of all the engine torque does not catch the inertia effect of a rotating shaft/propeller. The engine rotation rate vector is recalled and denoted $\vec{\Omega}_{E,e} = \vec{\Omega}_E \vec{x}_E$. The shaft inertia is denoted as J_E . The angular momentum of the rotating shaft is given in the engine frame

$$\vec{\mathcal{H}}_{p,e} = \vec{\Omega}_E J_E \vec{x}_E$$

The latter is illustrated on the figure 13. Considering the rotation speed constant its torque is given by

$$\Delta \vec{M}_{E,e} = \frac{d \vec{\Omega}_E}{dt} J_E \vec{x}_E + \vec{\Omega}_E J_E \frac{d \vec{x}_E}{dt} = \vec{\Omega}_E J_E \frac{d \vec{x}_E}{dt}$$

Thus the torque induced by the angular momentum does not depend on the angular acceleration. The previous line illustrated the idea, and now a more general case will derive. From now one, $\mathcal{H}_{p,l}$ is denoting the point mass angular momentum expressed in the local frame as follows

$$\mathcal{H}_{p,b} = [T]^T [T_0] \begin{pmatrix} H_{x_p,0} \\ H_{y_p,0} \\ H_{z_p,0} \end{pmatrix}$$

where $[T_0]$ is the unloaded transformation matrix evaluated at the spanwise location where the point mass is attached. That being said, the torque induced by

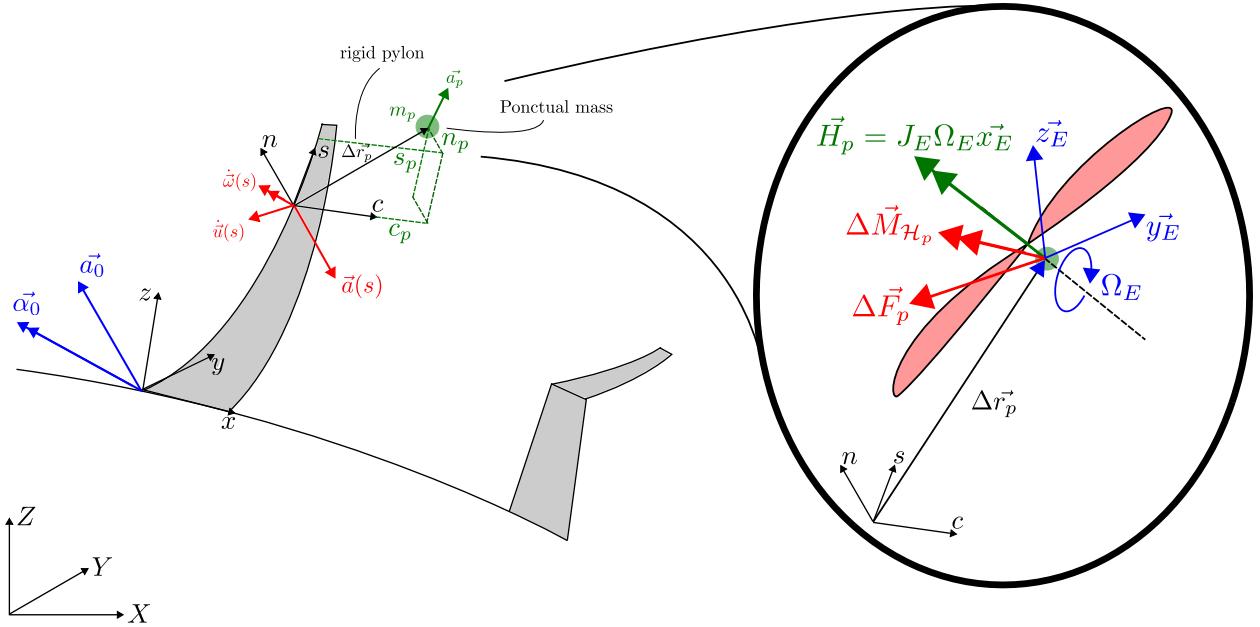


Figure 13: Ponctual mass rigidly connected to the local frame (left). Angular momentum of an engine (right), directions of the vectors are arbitrary

the angular momentum is given in the body frame.

$$\Delta \vec{M}_{\mathcal{H}_p} = -(\vec{\Omega} + \vec{\omega}) \times \vec{H}_{p,b}$$

Now let us consider that the point mass is rigidly attached to the local frame having a relative position to it

$$\Delta \vec{r}_{p,b} = [T]^T \Delta \vec{r}_{p,b} = [T]^T [T_0] (x_0, y_0, z_0)^T$$

The inertia and gravity loads of the punctual mass are given

$$\Delta \vec{F}_b = m_p (\vec{g} - \vec{a}_p) \quad (44)$$

where \$m_p\$ is the punctual mass, and \$\vec{a}_p\$ the acceleration relative to the inertial frame computed using equation 9. From the equation 44, the point mass moment about the csn origin and expressed in the body frame is given as follows

$$\Delta \vec{M}_{p,b} = \Delta \vec{r}_{p,b} \times \Delta \vec{F}_p - (\vec{\Omega} + \vec{\omega}) \times \vec{H}_{p,b} \quad (45)$$

2.7 Beams connections

Another interesting feature proposed by the ASWING structural model is the implementation of multiple beam objects. The beams are connected to each other using "restrictive" or "spring/compliant" joints. They are inherently massless and can be virtually connected to distant beams with a rigid pylon. Restrictive joints ensure that the compliant connection and orientation between the beams is maintained throughout the simulation. Each joint has 12 variables associated with it, i.e. position, orientation, forces and moments. Elastic

hinges are used to allow a degree of freedom between the beams. Note that Willis et al. (2007) used an unpublished modification of the code to prescribe motion between beams. Their work showed that they could reproduce the behaviour of a flapping bird in ASWING. The figures 14 (a) and (b) show the geometry they used at 2 different snapshots. It can clearly be seen that the orientation of the hinge axis has been specified. This feature will be presented in the aeroelastic part of this evaluation. Figure 14 (c) shows the use of elastic struts on the MIT Daedalus human prototype (Drela 1990 and 1988). Finally, figure 14 (d) shows the most common beam connection with the MICADO prototype Krengel et al. (2019).

2.8 Discretization of the problem

The equations 7, 8, 22, 23, 40 and 41 form a set of 18 non-linear differential equations with 18 unknowns, namely \$(\vec{r}, \vec{\theta}, \vec{u}, \vec{\omega}, \vec{F}, \vec{M})\$. The latter are continuous functions in \$s\$, but no analytical solution to the above set of equations has yet been found in the literature. Therefore, the problem has to be discretised. For the sake of clarity, a single beam is considered. Also, the distributed and point loads/momenta are considered as prescribed (i.e. not a function of the state vector). The beam is discretised into \$N_b\$ nodes using a cosine clustering function. This refines the beam tip and root where high curvature/deflection is expected. However, it results in a finite element problem with \$Nb \times 18\$ unknowns and the same number of non-linear differential equations. Note that during the

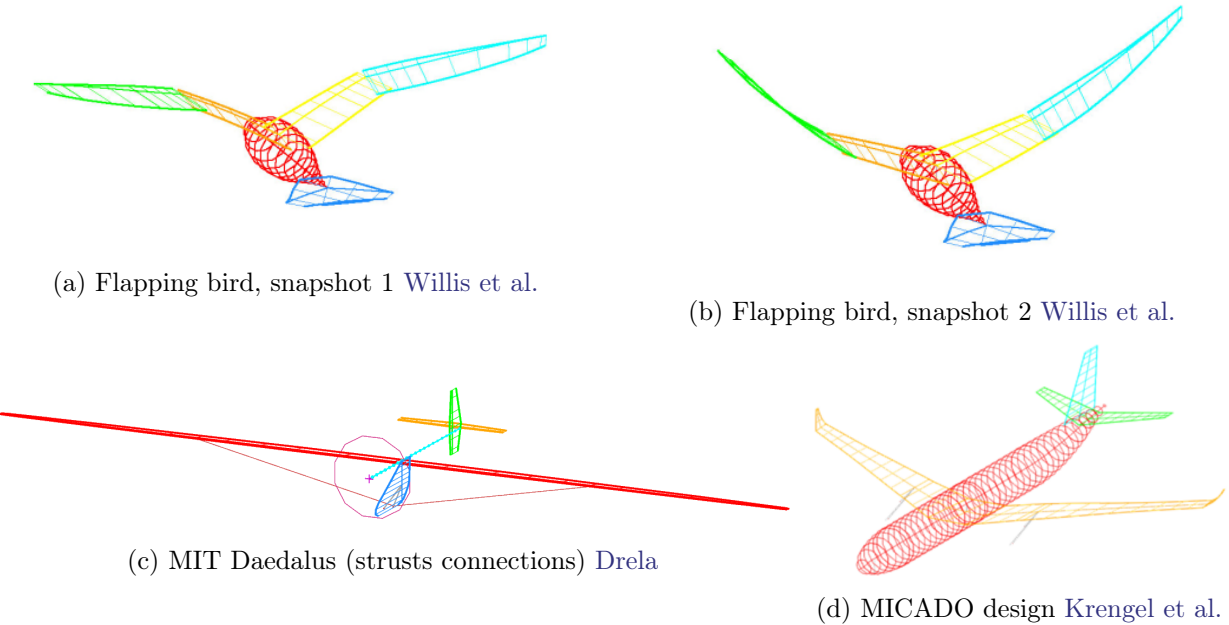


Figure 14: Examples of geometries implementable in ASWING

discretisation process all non-linear differential equations are pre-multiplied by the small element length ds . This effectively allows a zero length interval, as the latter is no longer the denominator of any $\frac{d}{ds}$ term, which would otherwise lead to numerical divergence. Thus the punctual forces/momenta are captured as a pure discontinuity as shown in figure 15. Unlike the aerodynamic model, it is not necessary to impose $Nb \times 18$ constraints to have a well-posed system of equations. The boundary conditions are simple: two free forces/momenta are imposed at the beam tip, plus ground or joint constraints on position, local velocity, orientation and rate of rotation. The latter are illustrated in the figure 15.

2.9 Structural failure analysis

ASWING offers an embedded function for structural failure analysis. In fact, maximum strains and torsional shear stress distributions can be calculated and reported. The latter can be compared with the maximum strains of the wing material to conclude whether the structure would fail under the specified applied load. The maximum extensional shear stress is expressed in ASWING as

$$\epsilon_{s,max}(s) = |c_{sh}\kappa_n| + |n_{sh}\kappa_c| + |F_s/EA| \quad (46)$$

where c_{sh} and n_{sh} are the relative coordinates to the stress axis of any point on the wing surface. The above equation can be considered conservative by its positive definition. In fact, materials may have different maximum strains in compression and extension. Or parts

of the wing are very likely to work in compression, such as the lee side of the wing. This small limitation can be overcome as (M'_c, M'_s, M'_n) and (F_c, F_s, F_n) distributions are also provided by ASWING for post-treatment. Using the curvature load relations 40 and 41 the curvature can be used to recover the induced strains. This would provide information on which materials in the section are under compression or extension and whether it is close to failure. As the latter may have different maximum extension/compression strains, the use of this technique would provide a better insight into which specific element of the section should be reinforced.

2.10 Column buckling analysis of non uniform beams

New types of architectures such as strut-braced or diamond/joined wing rise new types of problems, because some of their structural components work in compression and can be subject to buckling.

General concept: The divergence due to buckling is defined by a critical axial load applied on a straight beam. This load defines the moment when an out of plane local displacement is applied (cf figure 16), the beam is no longer able to resist the bending moment induced by the axial load, using its structural bending stiffness properties. When the properties are non axis-symmetric, the divergence occurs in the plane of the weakest bending stiffness property. The temporal response of the lateral displacement $\delta_x(t)$ is defined as a non harmonic divergence response. Thus from

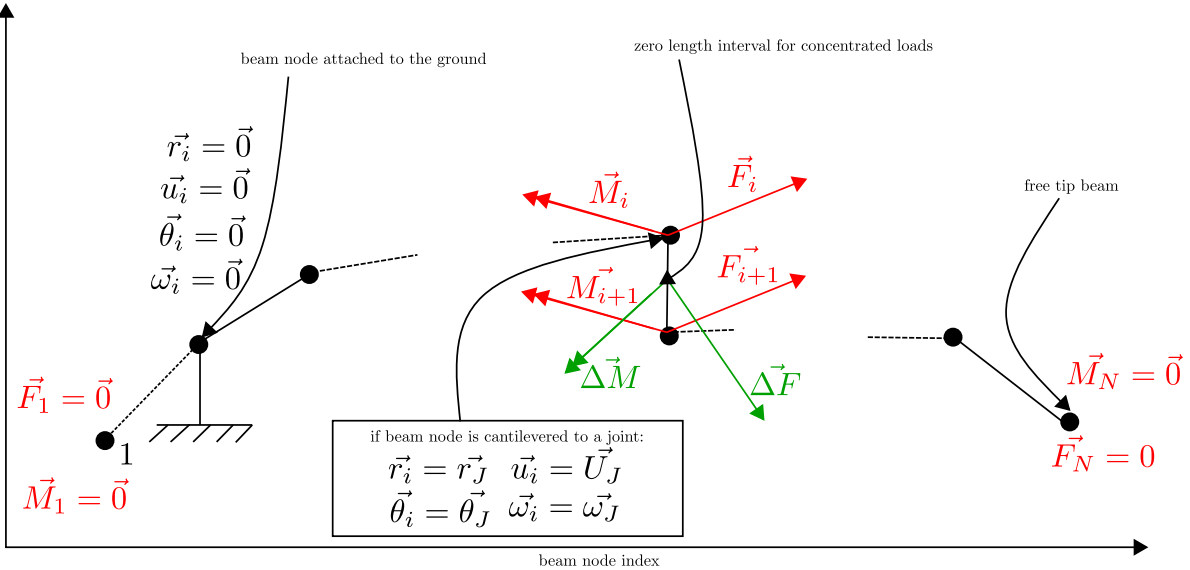


Figure 15: Concentrated load on zero length interval captured as perfect discontinuity. Beam constraints imposed at free tip joint and ground attachment

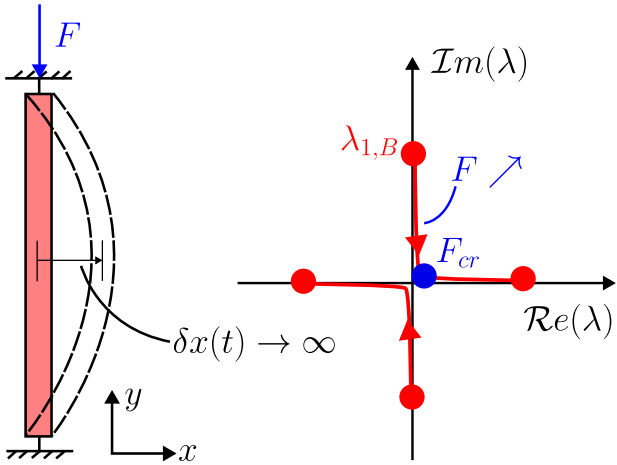


Figure 16: Buckling principle illustration, and detection through modal analysis

3 Numerical scheme convergence and time computation

Three different types of numerical analysis are possible in ASWING: modal/frequency, steady state and time marching. The latter do not use the same solver. Firstly, linear modal analysis involves an analysis of the linearised Jacobian matrix of the system. As its size can increase rapidly with mesh refinement, the eigenvalue problem cannot be solved by direct methods. Instead, an Arnoldi iteration method is used to compute the first modes of the system using the ARPACK library from Lehoucq et al. (1998). The steady and transient structural behaviour is computed using a Newton descent algorithm whose main computational complexity comes from the inversion of the steady/transient Jacobian matrix of the following nonlinear constrained system below

$$r(\dot{x}, x, u) = 0 \quad (47)$$

where r is the set of ordinary nonlinear differential equations of the system, x is the system discrete state vector, and u is the exogenous input vector. The latter inversion solver follows a specific pattern, so the complexity is not in n^3 . Thus ASWING uses 2 solvers so, 2 mesh convergence comparisons have been performed. For the Newton descent algorithm, 3 steady deflections were chosen as the convergence criterion, while for the Arnoldi iteration, the first 4 beam modes were chosen. In both cases, the number of structural nodes was multiplied by 2 from one case to the other. For each case the computation time was reported. Figures 17(a)-(c) show the degree of convergence of each variable considered in each solver analysis. Figure (c)

a modal analysis point of view, finding the critical load consists to find when a first pure real positive mode appears. Euler provides analytical solutions of this problem for various cantilevering cases of beams. However, the major problem is that, this solution is only for uniform beams which is generally not the case for aeroplane structure. Aswing models such beams and thus extend the Euler solution to more complex structure. In consequence, as long as the numerical mesh convergence is showed, Aswing will provide buckling critical load predictions.

particularly highlights the difference in computational complexity of the different solvers. Overall, 40 nodes per beam provide acceptable results for a reasonable computational time.

4 Experimental Validation

This section aims to provide a partial validation of the features of the ASWING structural model. These include the nonlinear static deflections and the modal response predictions. Four sets of experiments were used. Minguet (1989, 1990a and 1990b) present high deflections and modal response of helicopter blades. The latter is considered as a baseline set as the aspect ratio of the sample is quite high ($AR = 20$). The evaluation is refined by slowly reducing the test cases aspect ratio. To this end, the Pazy Wing of Avin et al. (2022) is employed, with a wing aspect ratio of 5.5. A "boundary" case is then used to highlight the structural model limits in terms of aspect ratio. To do this, data from Dunn and Dugundji (1992 and 1992) are used, again evaluating static deflections and modal response predictions for a wing with aspect ratio 4. Then, a fourth "boundary" case is used to study the effect of concentrated mass on the modal response of a straight wing (AR of 6). The latter case from Runyan and Sewall (1948) does not provide static deflection data. After that, a fifth case is used to assess the effect of various joint on the static response of a joined wing using NASA's data (Lin et al.-1989). The sixth case proposes a discussion on the Aswing capacity to predict column buckling critical load, by invoking Euler's solution and the experimental work of Niles (1946). Every cases and their purposes are summarized in table 2.

4.1 CASE ST-1: Static deflection and modal response of high aspect ratio helicopter blades

CASE ST-1: experimental bench:

In this work, the static tip deflections of 4 different blades were investigated for various tip loads. Their modal response up to the 5th mode was also evaluated. An experimental bench was set up for this purpose (see figure 18). Each blade was rigidly cantilevered from an aluminium clamping device. The blade length and chord were 0.55m and 0.03 m respectively, for an aspect ratio of approximately 20. The stiffness and mass properties of each blade are given in tables 7, 8 and 9. For static deflection, the tests consisted of attaching a mass to the tip of the blade on the half chord axis. The mass varied from 0 to 0.5 kg,

with increments of 0.1 kg for high deflections and 0.05 kg for low deflections. A millimetre ruler was used to measure the tip deflections. As the blades were initially horizontally cantilevered and quite flexible, they bent under their own weight. Minguet provided relative data (difference between loaded and unloaded beams). Finally, the clamping system could be rotated against the spanwise axis at 3 different angles, i.e. $\theta = (-45^\circ, 0^\circ, 45^\circ)$, allowing the effect of stiffness coupling terms on the measurements to be captured. For the modal analysis, each blade was in the configuration $\theta = 0^\circ$ and unloaded. An electromagnetic shaker was attached to the blade near the root (50mm from the root) but slightly off the half-chord axis to excite the torsional mode. A strain gauge was attached at the same location and connected to a digital oscilloscope. The shaker was controlled by a frequency generator, which was also the first input to the oscilloscope. By looping the strain gauge signal, they could see when the beam was in resonance (Lissajou figures). In total, up to 5 modes could be precisely identified.

CASE ST-1: numerical analysis: The numerical analysis was split into two parts. Firstly, the tip deflections were studied by replicating the bench and applying tip loads through puntual masses derived from the theoretical section. Numerical sensors were located at the trailing and leading edge, in the same positions as the experiments. Subsequently, unloaded and loaded deflections were measured. A separate ASWING file was produced for each blade configuration, using the parameters retrieved from tables 7, 8, and 9. To ensure numerical convergence, 40 structural nodes were clustered according to a cosine function. The blade was geometrically twisted by θ to model the clamping system rotation. Note that during the crafting process, one of the blades became naturally twisted ($[45/0]_{3a}$). This was taken into account during the ASWING analysis. For the modal analysis, the point mass and root twist were eliminated, and the non-linear equations were solved using the OPER menu to produce a steady-state solution. Next, a modal analysis was conducted on the Jacobian matrix of the linearized system in the MODE menu. The first five modes were computed quickly thanks to the Arnoldi algorithm that is implemented natively. Again, based on mesh convergence analysis, 40 structural nodes were utilized to execute all modal analyses.

CASE ST-1: Results: The analysis begins with comments on static deflection predictions. Four laminates were selected overall to evaluate a specific feature of the structural model.

The first laminate examined, $[0/90]_{3s}$, serves as a baseline case with only c and s bending stiffness coef-

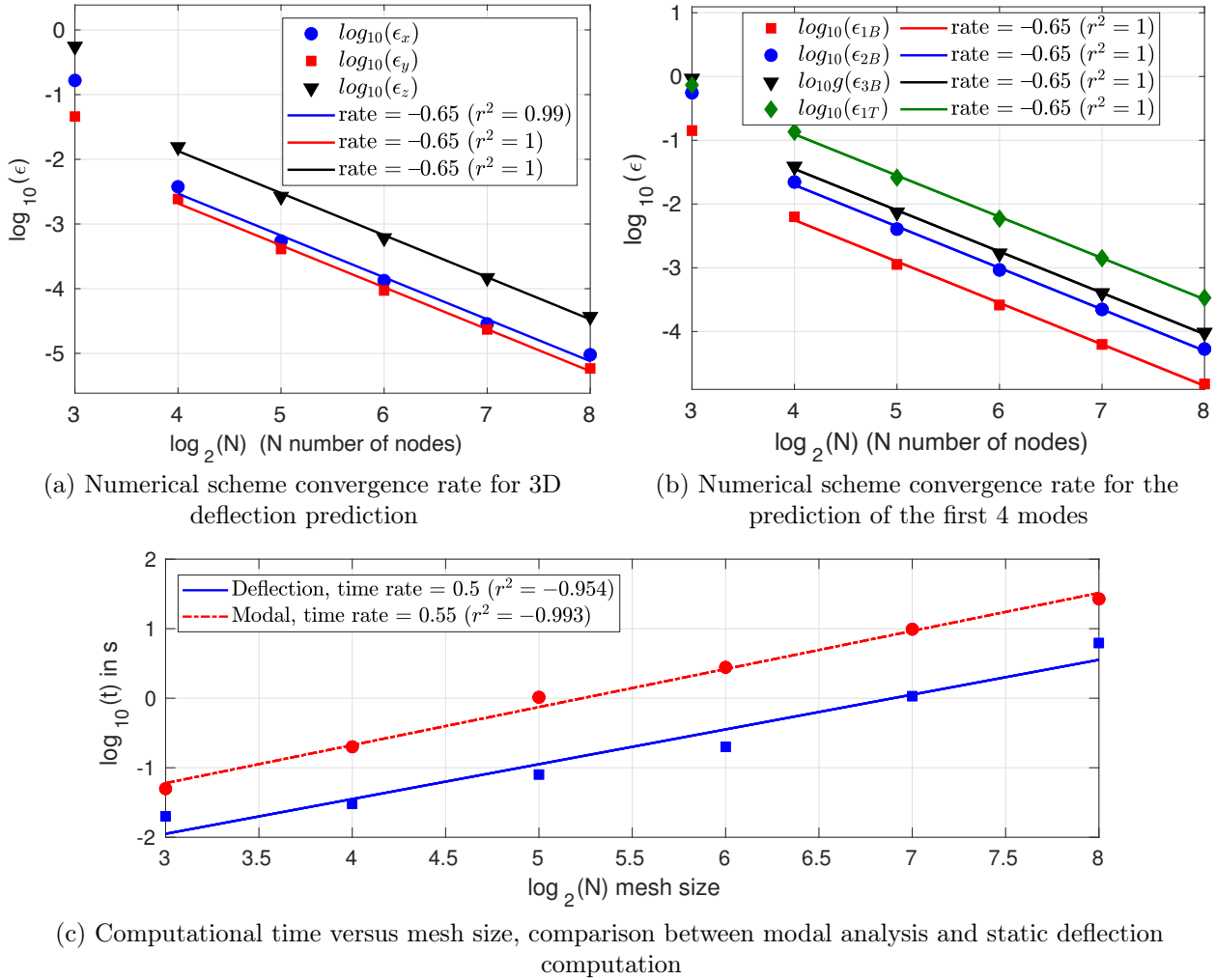


Figure 17: Structural model numerical scheme performances

Table 2: Experimental evaluation cases. $\mathcal{ST} = \mathcal{S}\mathcal{T}$ ructural cases.

CASE	Geometry	Exp data	Evaluation type
\mathcal{ST} -1.A-E	Helicopter blades (5 composite layouts)	[37, 38, 39]	Large static deflection (A to D only) and modal response (A to E). Effect of different bending/torsion coupling terms. High-aspect ratio.
\mathcal{ST} -2.A-B	Pazy wing (isotropic material)	[2]	Large static deflection and modal response. Effect of the skin on torsion prediction. Moderate aspect ratio.
\mathcal{ST} -3.A-C	Straight wing (3 composite layouts)	[19, 20]	Large static deflection and modal response. Effect of different bending/torsion coupling terms Low-aspect ratio.
\mathcal{ST} -4	Straight wing (isotropic material)	[47]	Effect of a tank /nacelle lateral and longitudinal on the modal response of a straight wing Moderate-aspect ratio.
\mathcal{ST} -5.A-B	Joined wing JWRA Nasa prototype (isotropic material)	[35, 49]	Out of plane bending moment spanwise distribution prediction. Effect of 2 joint with different degrees of freedom. Moderate aspect-ratio.
\mathcal{ST} -6.A-E	Column buckling	[40]	Column buckling prediction Effect of the effective slenderness ratio

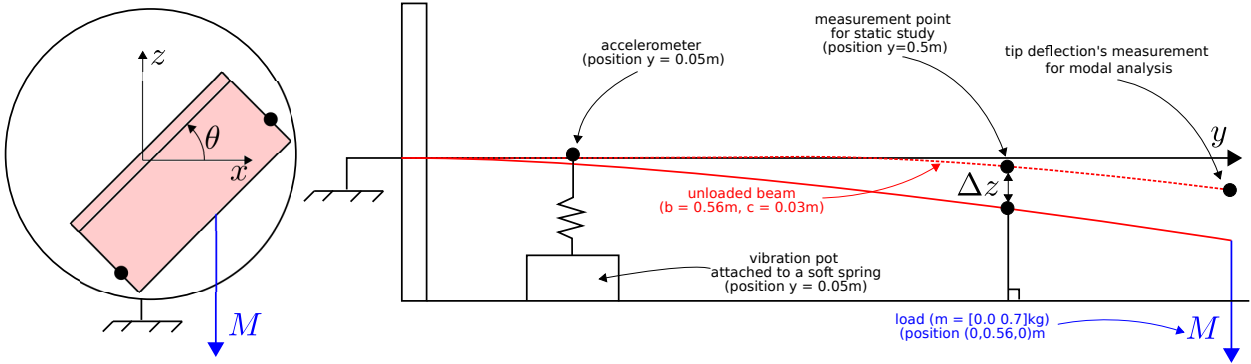


Figure 18: CASE ST-1: experimental bench description

ficients (EI_{cc} , GJ). From the non-coupling property of its stiffness matrix, only one blade root inclination was necessary ($\theta = 45^\circ$). The non-zero inclination was primarily used to measure x deflections. Figures 19 (a) and (b) depict the (x , y , z) relative predictions against experimental data. In both cases, ASWING accurately captured the non-linear deflections for high tip loads. Furthermore, the x deflection was in excellent agreement with the experimental results when the wing was twisted.

The purpose of the second laminate ($[20/-70/-70/20]_{2a}$) is to investigate whether omitting certain stiffness matrix coefficients, as done in the theoretical development, could lead to problems. In such a scenario, the layout exhibits a coupling between an extension in the s direction and a chordwise torsion (E_{25}). Since no bending coupling terms are present, the situation is regarded as symmetrical and only two root twists were taken into consideration ($\theta = 0^\circ$, $\theta = 45^\circ$). The graphs in Figures 22 (a) and (b) illustrate the predicted relative deflections in the x , y , and z directions. Notably, the prediction for the z direction is highly accurate when compared to the experimental data. It is worth noting that despite the omission of the E_{25} coefficient in the numerical model, the prediction errors are similar to those of the initial layout.

The third laminate ($[45/0]_{3s}$) was selected to introduce the bending coupling term, specifically the chordwise and spanwise bending coupling terms. To clearly observe its impact, three angles of rotation at the roots were evaluated ($\theta = -45^\circ$, $\theta = 0^\circ$, $\theta = 45^\circ$). The numerical predictions are shown in figure 21 (a) to (c). It is noteworthy that when the wing is flat, the x deflection is non-zero. If the non-zero root angle is taken into account, the latter change is not symmetrical because of bending torsion coupling. This characteristic is effectively modelled by ASWING. Although the y deflection is slightly weaker, it is still in good agreement. In terms of aerodynamics, spanwise deflection (y) has less of an impact than deflection in

the z or x directions.

The fourth case ($[45/0]_{3a}$) shares similarities with the first, except for a twisted tip resulting from the crafting process. Figure 22 (a) and (b) illustrate the satisfactory agreements with experiments of every tip displacement component.

Modal analysis was conducted on three laminates that have been previously introduced, namely ($[0/90]_{3s}$, $[45/0]_{3s}$ and $[20/-70]_{2a}$). The fourth case was selected to highlight the potential issue arising with highly flexible blades. The ASWING predictions, along with their discrepancies against experimental data, have been presented in table 3. The last two rows of the table showcase a highly flexible blade, with tests performed in face down and up configurations. A huge asymmetrical effect on the wing tip deflection has been witnessed by the author. And at the light of the first torsion mode column, this asymmetry has an impact on rising the ASWING prediction error from one configuration to another. The author reported that this asymmetry was mainly due to manufacturing limits, as the blade was extremely thin in comparison to the others. Moreover, this case is very stressful and is impossible to witness in reality as it is too flexible and would break under any aerodynamic loads. Nevertheless, commentary can be provided for the first three laminates. Firstly, the forecasts align excellently with the experiments. The highest forecast error is below 10% and has an average of 7% for the first three bending modes. While slightly inferior for the torsion, it is still reasonable. Note that ASWING accurately captures the impact of a coupling term that affects the first torsion mode, resulting in improved decoupling between the first bending and torsion modes. Since these modes are typically associated with flutter, using the $[45/0]_{3s}$ and $[20/-70]_{2a}$ laminate should lead to a greater flutter robustness, despite having the same bending stiffness properties as the $[0/90]_{3s}$ laminate.

Based on the initial outcomes, ASWING demon-

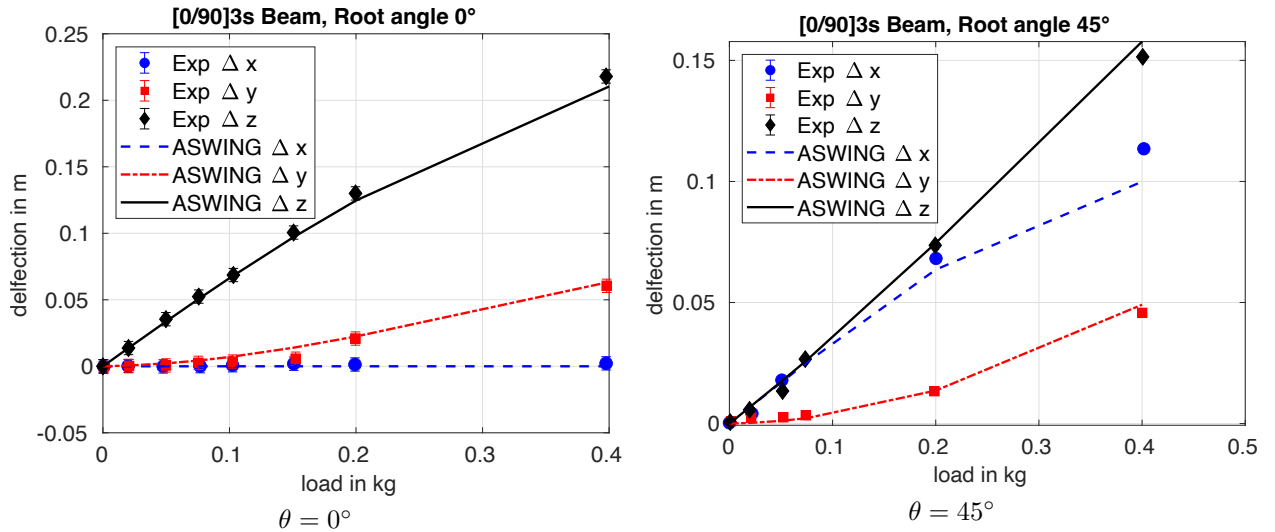


Figure 19: CASE ST-1.A, layout : [0/90]3s ($\Delta_x, \Delta_y, \Delta_z$) predictions against experiments from Minguet 1989

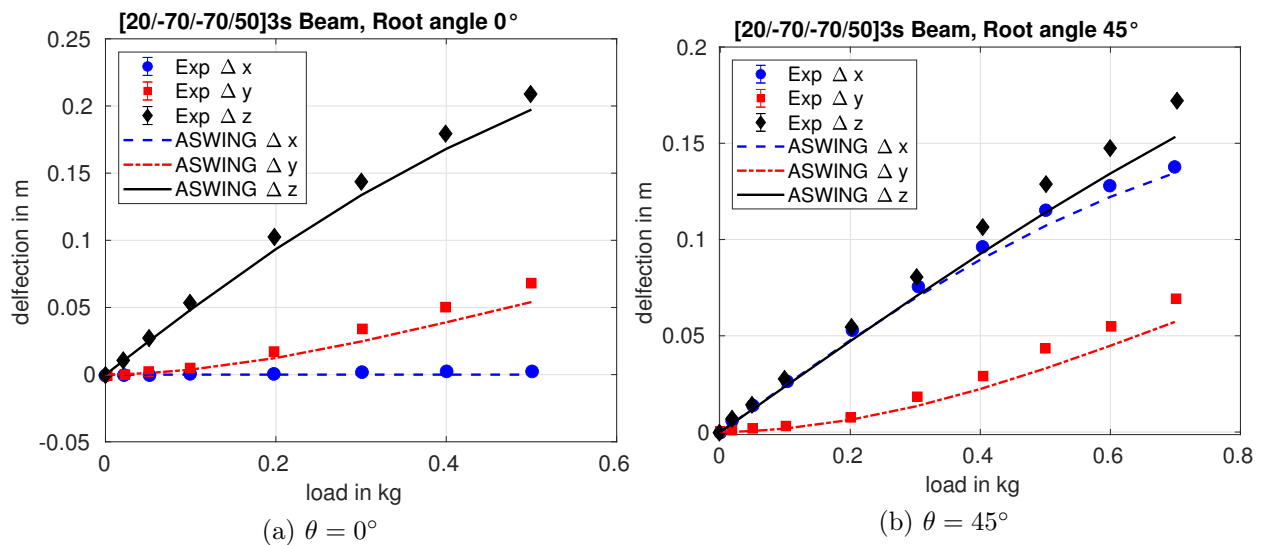


Figure 20: CASE ST-1.B, layout : [20/-70/-70/20]2a, tip ($\Delta_x, \Delta_y, \Delta_z$) predictions against experiments from Minguet 1989

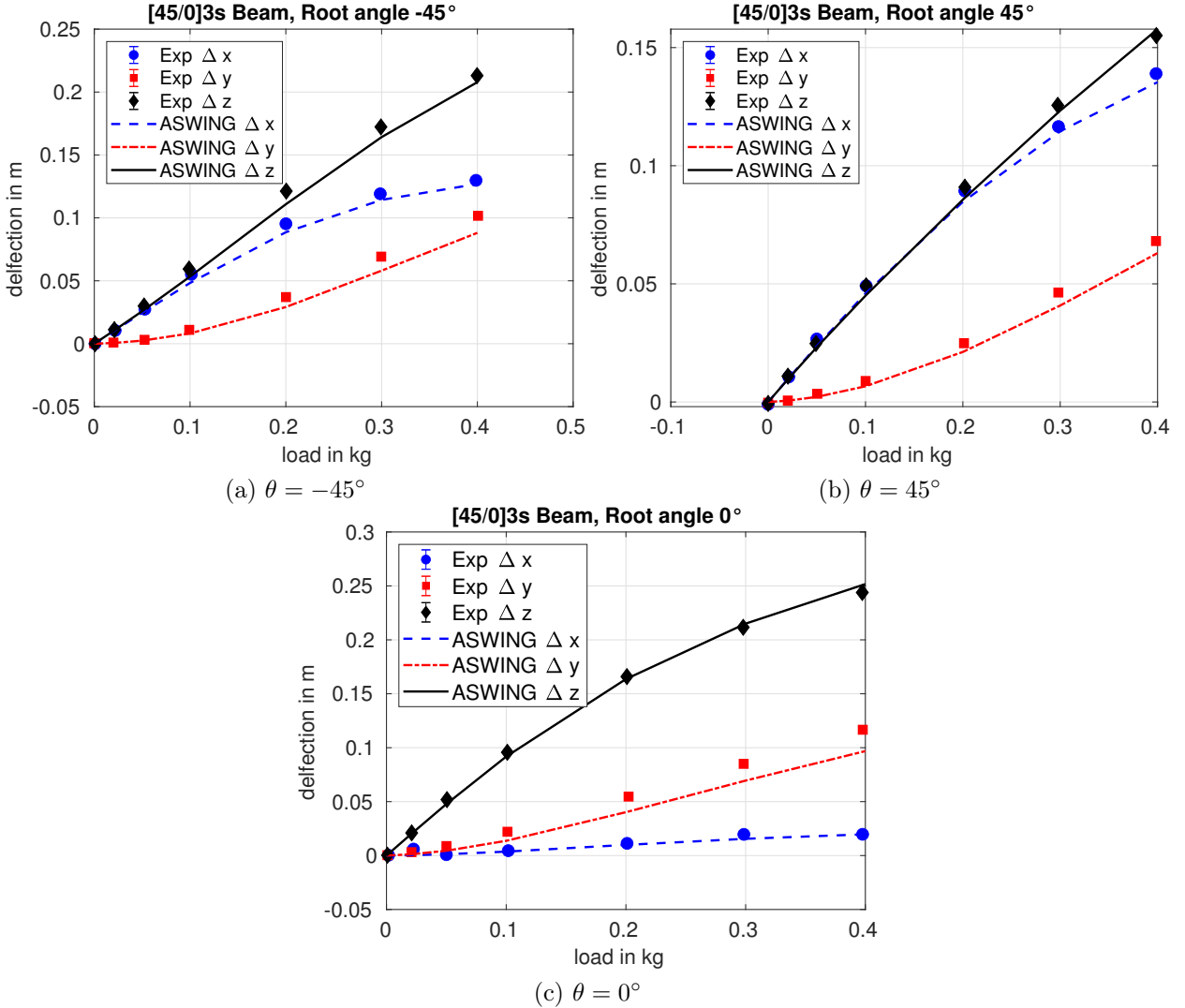


Figure 21: CASE \mathcal{ST} -1.C, layout : [45/0]3s, tip ($\Delta_x, \Delta_y, \Delta_z$) predictions against experiments from Minguet 1989

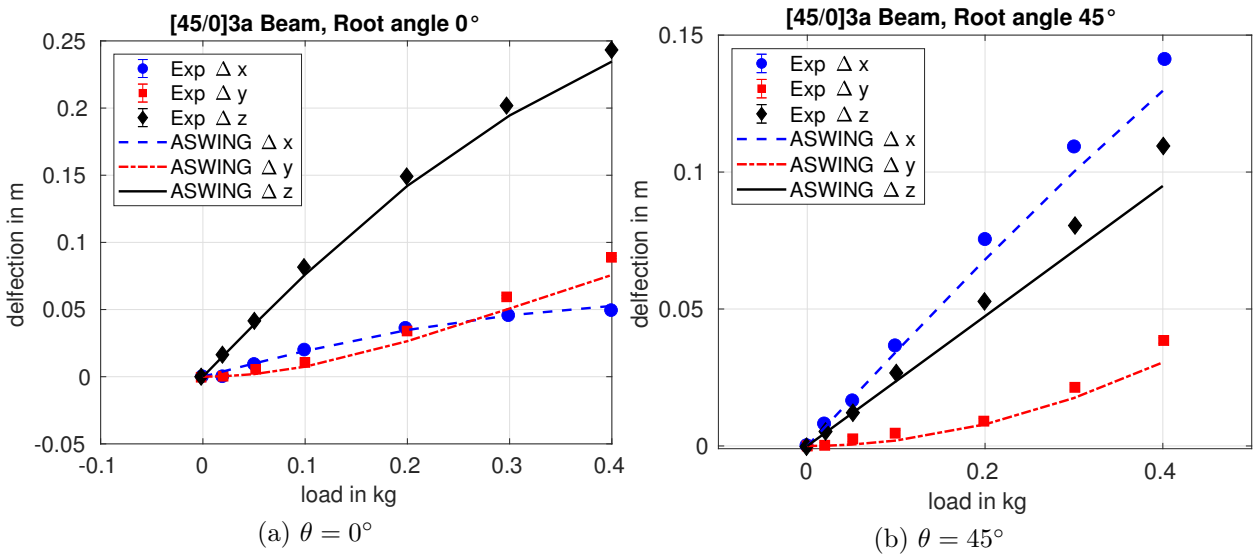


Figure 22: CASE \mathcal{ST} -1.D, layout : [45/0]3a ($\Delta_x, \Delta_y, \Delta_z$) predictions against experiments from Minguet 1989

strated good modal and deflection prediction performances for different composite layouts of helicopter blades. Nevertheless, this specific dataset does not sufficiently test the efficacy of the structural model mainly due to the high aspect ratio of the blade. However, the said attribute has been preserved since it exhibited intriguing characteristics that were absent in situations with lower aspect ratios. Two of the measurements taken were the 3D non-linear large deflections and high-frequency modes. The following sections will present the validation analysis using two moderate to low aspect ratio wings.

4.2 CASE ST-2 : Static deflection and modal response on a moderate aspect ratio wing:

The previous cases pose no real stress on the theoretical model as they only present a high aspect ratio. The assessment is therefore refined to a lower one, in order to more accurately capture the limits. To this end, the Pazy Wing of [Avin et al. \(2022\)](#) is employed, with a wing aspect ratio of 5.5. For further information on the wing's design, please refer to [Avin et al.'s](#) articles.

CASE ST-2: experimental Setup:

The wing is clamped. To prevent torsion to be involved, a mass is positioned on the mid chord wing tip for tip deflection measurements as shown in Figure 23-a. The structure is constructed from a flat aluminium plate covered with a shell. As the elastic axis is approximately located at 44% of the chord, placing the mass at mid chord is improbable to involve torsion. For tip torsion measurements, the mass is again located at the tip, but with a chordwise offset (see figure 23-d). The offset is fixed at 0.08m from the leading edge of the wing tip. The tip mass is adjusted to achieve a 50% span tip deflection, regardless of the configuration. The tip deflections are measured at the mid-chord, while the tip torsion is calculated from the differential vertical and lateral position of the leading and trailing edges. Deflection tests have been conducted both with and without the skin (see figures 23 a and b). Additionally, ground vibration tests have been carried out in both vertical and horizontal positions, which are denoted as undeformed and deformed configurations.

CASE ST-2: numerical Bench:

The Pazy wing has been replicated in ASWING using stiffness, mass, and inertia per unit length data provided by [Riso and Cesnik \(2023\)](#). Tip masses have been attached at the given positions with three sensors placed at the leading, trailing, and mid-chord edges. The implementation consists of forty structural nodes, guaranteeing converged forecasts. For the purpose

of modal analysis, two files were generated: one for the Pazy wing in the vertical position (un-deformed) and another for the wing in the horizontal position (deformed on its own weight).

CASE ST-2: results:

Figures 23 (a) to (f) display the deflection predictions for the "bending" bench (mass at mid-chord) and "torsion" bench (mass forward of the leading edge). The comparison between ASWING predictions and UM/NAST results from [Riso](#) and [Cesnik-2023](#) shows a high level of agreement. The presented error in predictions is solely for ASWING. Remarkably, the tip deflection follows experimental measurements with predictions errors lower than 10%, even at large deflections, irrespective of whether the skin is on or off. In terms of the tip twist, ASWING achieves excellent agreement with experimental measurements when the wing skin is off, with prediction errors below 10% for large deflections. When the skin is attached, both UM/NAST and ASWING show poor predictions at high deflections. According to [Riso](#) and [Cesnik](#), this behaviour is due to challenges in modelling the wing skin behaviour during stretching and could partly result from measurement errors (estimated at up to 1.2 degrees for twist angle). The ASWING, UM/NAST and SHARPY predictions of the pazy wing modes are compared with the ground vibration tests of [Avin et al.](#) in the table 4. The first 3 out-of-plane (OOP) measurements are well captured by ASWING with a prediction error of less than 10% in each case. The first torsional mode is also well captured. Finally, the In Plane (IP) mode is not well captured with a prediction error greater than 200%. This is not really consistent with the Minguet bench results. Errors in the in plane stiffness or inertia estimation could explain such discrepancies. Also from an aeroelastic point of view, such a mode is poorly energetic due to the large difference between the chordwise and normal stiffnesses. Furthermore, the aerodynamic loads are very unlikely to excite an in-plane mode. Consequently, the discrepancies in the predictions for these modes are not that important. Finally, according to the predictions of the other model (UM/NAST and Sharpy), ASWING presents similar results.

Overall, for moderate aspect ratios, the ASWING predictions are still in good agreement with the experiments. At high deflections the twist predictions start to show weakness, but the results are still reasonable. The evaluation is then pushed further to really capture the limits of the model in terms of aspect ratio.

Layup	Type	w_{tip} , mm	1B, Hz	2B, Hz	3B, Hz	1T, Hz	1F, Hz
$[0/90]_{3s}$	Exp	20	5.7	34	98	62	
	ASW	1.2E-2	5.74	36	101	78	
	ϵ_1	40%	0.75 %	6.02 %	3.4 %	16%	
$[45/0]_{3s}$	Exp	18	4.3	28	78	135	
	ASW	17	4.75	29.81	83.7	95.0	
	ϵ_1	5.5 %	10 %	6.46 %	7.38 %	29 %	
$[20/-70]_{2a}$	Exp	12	5.8	36	103	166	
	ASW	11	5.86	36.8	103	187	
	ϵ_1	7.5 %	2.2 %	4.2 %	0 %	12 %	
$[45/0]_{s,u}$	Exp	137	1.4	8.0	20	68	10
	ASW	210	1.4	8.14	21.8	59	7.6
	ϵ_1	53 %	0 %	1.75 %	9 %	13 %	24 %
$[45/0]_{s,d}$	Exp	202	1.4	8.2	20	57	6.5
	ASW	210	1.4	8.14	218	59	7.6
	ϵ_1	3.9 %	0 %	0.7 %	9 %	3.3 %	16 %

Table 3: CASE ST-1.A-E: helicopter blades modal analysis against experiments (Minguet 1989)

Modes in (Hz)						
Configuration	Data	OOP1	OOP2	T1	IP1	OOP3
Undeformed	Exp	4.26	28.5	42.0	60.7	81.5
	ASWING	4.59	29.1	43.4	128	81.4
	ϵ_A	7.7 %	2.1 %	3.3 %	+110 %	-0.1 %
	UM/NAST	4.19	28.5	41.9	83.1	105.89
	ϵ_U	-1.6 %	-0.02 %	-0.1 %	1.7 %	73 %
Deformed	Exp	4.39	29.8	41.0	N/A	82.5
	ASWING	4.67	29.2	43.2	116	81.4
	ϵ_A	6.4 %	-2 %	5.36 %	NC	-1.3 %
	UM/NAST	4.19	28.5	41.6	100.1	83.03
	ϵ_U	-4.6 %	-4.4 %	1.4 %	NC	NC
	SHARPY	4.69	30.87	43.71	NC	88.19
	ϵ_S	6.8 %	3.7 %	6.6 %	NC	6.9 %

Table 4: CASE ST-2.A (skin off): Pazy wing modal response in undeformed and deformed condition. ASWING, UM/NAST (Riso and Cesnik-2023), Sharpy (Goizueta et al.-2022) predictions against experimental data (Avin et al.-2022)

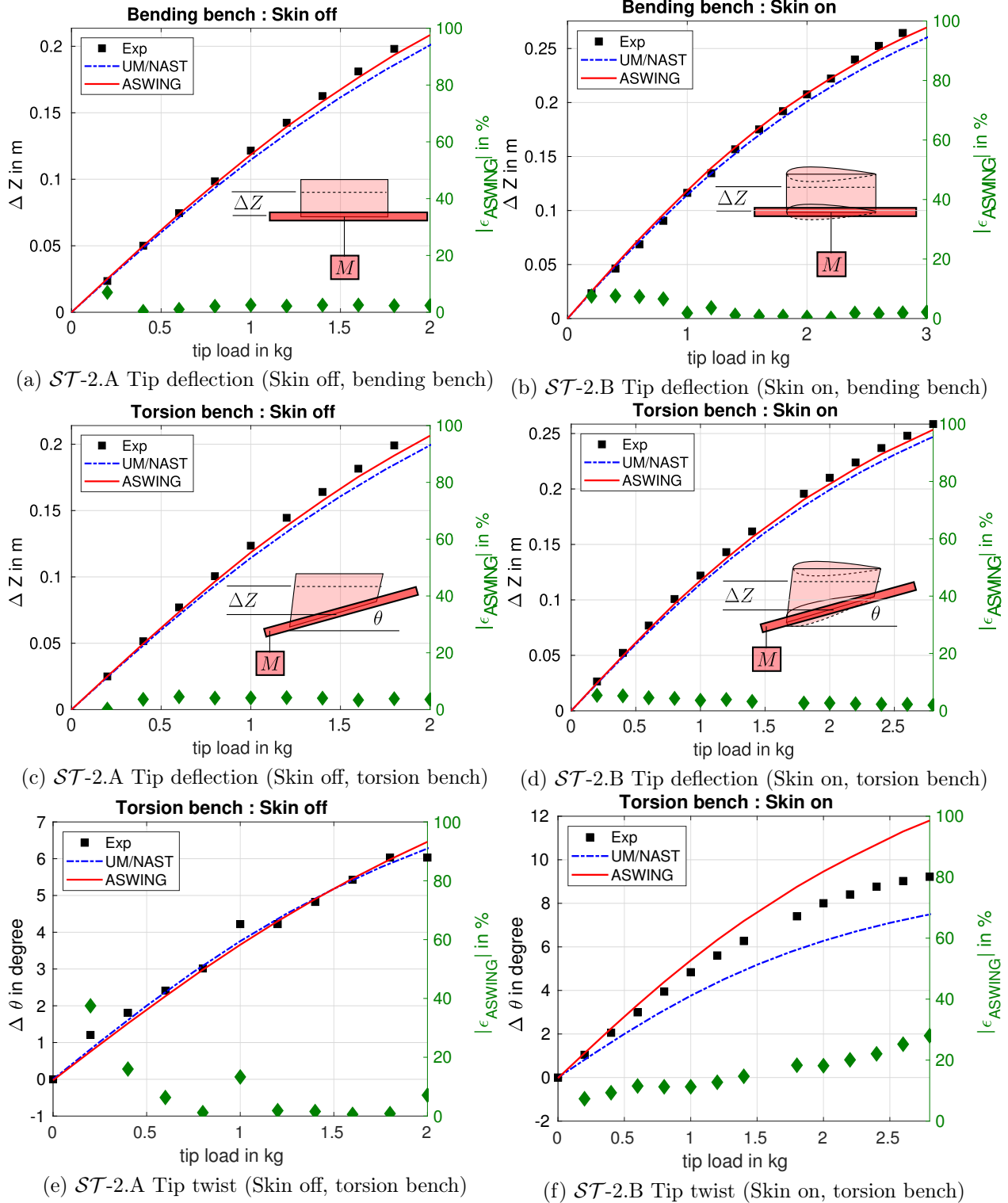


Figure 23: CASE \mathcal{ST} -2.A-B: Pazy wing static deflection and twist. ASWING predictions against UM/NAST (Riso and Cesnik-2023) and experimental data (Avin et al.-2022)

4.3 CASE ST-3: static deflection and modal response of low aspect ratio wings : boundary case

In order to clearly identify the limits of the model, the aspect ratio of the test cases needs to be lowered again. This last case is adapted from the work of Landsberger (1983), Landsberger and Dugundji, (1985), Dunn (1992) and Dunn and Dugundji (1992) where several aeroelastic experimental analyses have been carried out.

CASE ST-3: experimental setup:

The wing is made of a flat 6-ply composite plate with polystyrene fairings glued to it to reproduce a NACA0012 shape. A total of 3 wings have been built with 3 different composite layouts with different stiffness couplings. The latter was adapted to the ASWING formalism and derived in the tab 10. The aspect ratio of each wing was 4, making them excellent stress cases for the ASWING structural model. Each wing was cantilevered on an aluminium clamping device as shown in figure 24. For static quantification, 2 rulers were placed very close to the leading and trailing edges of the wing tip. Their accuracy was about 0.1 mm. A force was applied to the wing tip at the half chord line using a mass pulley system. A moment was applied around the half chord line using 2 mass pulley systems connected to the leading and trailing edges. Both have opposite directions and equal masses. The force was increased in steps of 100g while the moment was increased by 20g. For the modal analysis, the test bench differs from the previous one. In fact, since the latter was mainly dedicated to flutter measurements, the modal analysis was carried out in the wind tunnel to check if the structure had been damaged from one run to the next. To do this, they used bending and torsion strain gauges connected to a digital oscilloscope to record the transient response of the structure. An impulse force was then applied between each run using a rod at the tip of the blade, away from the torsional axis. The impulse, which had a large bandwidth, exited the wing first natural modes. Through a Fast Fourier Transform analysis of the transient response, the 3 first natural mode frequencies were calculated and reported in the author's paper. Only the 2 first bending modes and 1 torsional mode could be calculated due to the typology of the bench. In fact, high frequency modes are very difficult to extract using this method and so their contribution to the transient response was probably lost in the measurement noise.

CASE ST-3: numerical bench: In spite of the helicopter blade bench, it was not possible to repro-

duce exactly the configuration in ASWING for the deflection measurements. In fact, since the wing is mounted vertically in this case, it is not possible to apply horizontal punctual forces. In ASWING, the wing is mounted horizontally and its inertial properties have been eliminated. For force measurements, a point mass was placed at the wing tip on the half chord line. For momentum predictions, the mass was attached to the trailing edge of the wing. Note that in both cases it is possible to implement a negative mass so that negative moments and forces can be implemented. In terms of modal analysis, the wing could be cantilevered vertically, so the same procedure as in the previous section was used with the same numerical parameters and conclusion on mesh convergence.

CASE ST-3: Results: Figure 25 (a) to (d) show the deflection and torsion predictions of ASWING against the experimental data. Contrary to the previous case, the agreement is not satisfactory, although the framework captures the tendency for a bending-torsion coupling. ASWING seems to be a bit weak for tip deflection (Figure 25 (a)). This highlights the limitations of structural model for wings/beams with an aspect ratio less than 4. Below, 3D finite element models should be considered, such as the predictions of Dunn shown in figure 25. Note that the development of such a modification in ASWING would be pointless if it will be still coupled to the lift line model. In fact, although the lifting line performance is expected to decrease rapidly as the aspect ratio squeezes. Consequently, a modification of the structural model would imply the use of a new aerodynamic one, such as the unsteady vortex/particle or lattice methods. The reader can take a look at the work of Drela et al. (2019) who has proposed such a solution.

The conclusion about the modal response of the cases is less severe. the frequency predictions are still reasonable. This could be explained by the small excitation configuration where the 3D shear stress coupling is expected to dominate. Obviously there is a decrease in prediction performance. Despite the poor tip and twist deflection predictions in this case, we will see in the aeroelastic part of this evaluation work that ASWING shows interesting results in this case and that the conclusion about the boundary limit of the model is not as severe as the one above.

4.4 CASE ST-4: Effect of a concentrated mass on the modal response of a straight wing

As seen in the theoretical section, it is possible to take into account the effect of point masses attached to any beam by means of a rigid pylon. This feature is

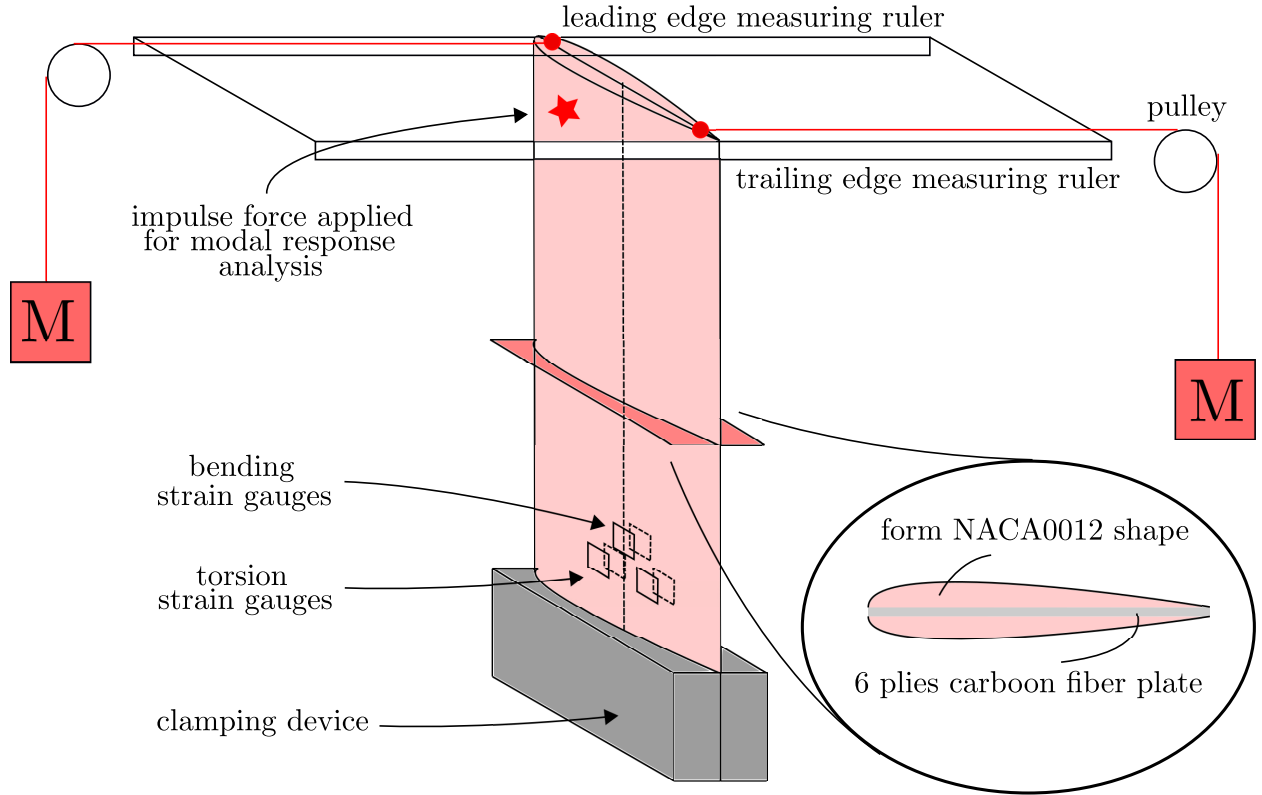


Figure 24: CASE ST-3: low aspect ratio wing, static deflection and modal response experimental bench Dunn

Layup	Type	1B (in Hz)	2B (in Hz)	1T (in Hz)
	<i>Exp</i>	4.0	27.1	21.4
	<i>ASWING</i>	3.7	24.3	25.9
$[0_3/90]_s$	ϵ_1	-7.5%	-10 %	25.9 %
	<i>P.E Dunn</i>	4.3	27.2	24.6
	ϵ_2	7.5 %	0.4 %	15 %
	<i>Exp</i>	3.6	22.7	27.1
	<i>ASWING</i>	3.63	22.5	26.6
$[+15_2/0_2]_s$	ϵ_1	0.9 %	-0.9 %	-1.8 %
	<i>P.E Dunn</i>	4.5	23.5	28.6
	ϵ_1	8.3%	3.5 %	5.5 %
	<i>Exp</i>	3.6	24.5	27.4
	<i>ASWING</i>	3.62	22.5	26.6
$[-15_2/0_2]_s$	ϵ_1	0.5%	-8.2 %	-2.9 %
	<i>P.E Dunn</i>	3.6	24.1	27.8
	ϵ_2	11.1 %	-1.6 %	1.5 %

Table 5: CASE ST-3.A-C: NACA0012 straight wing modal analysis Dunn (1992)

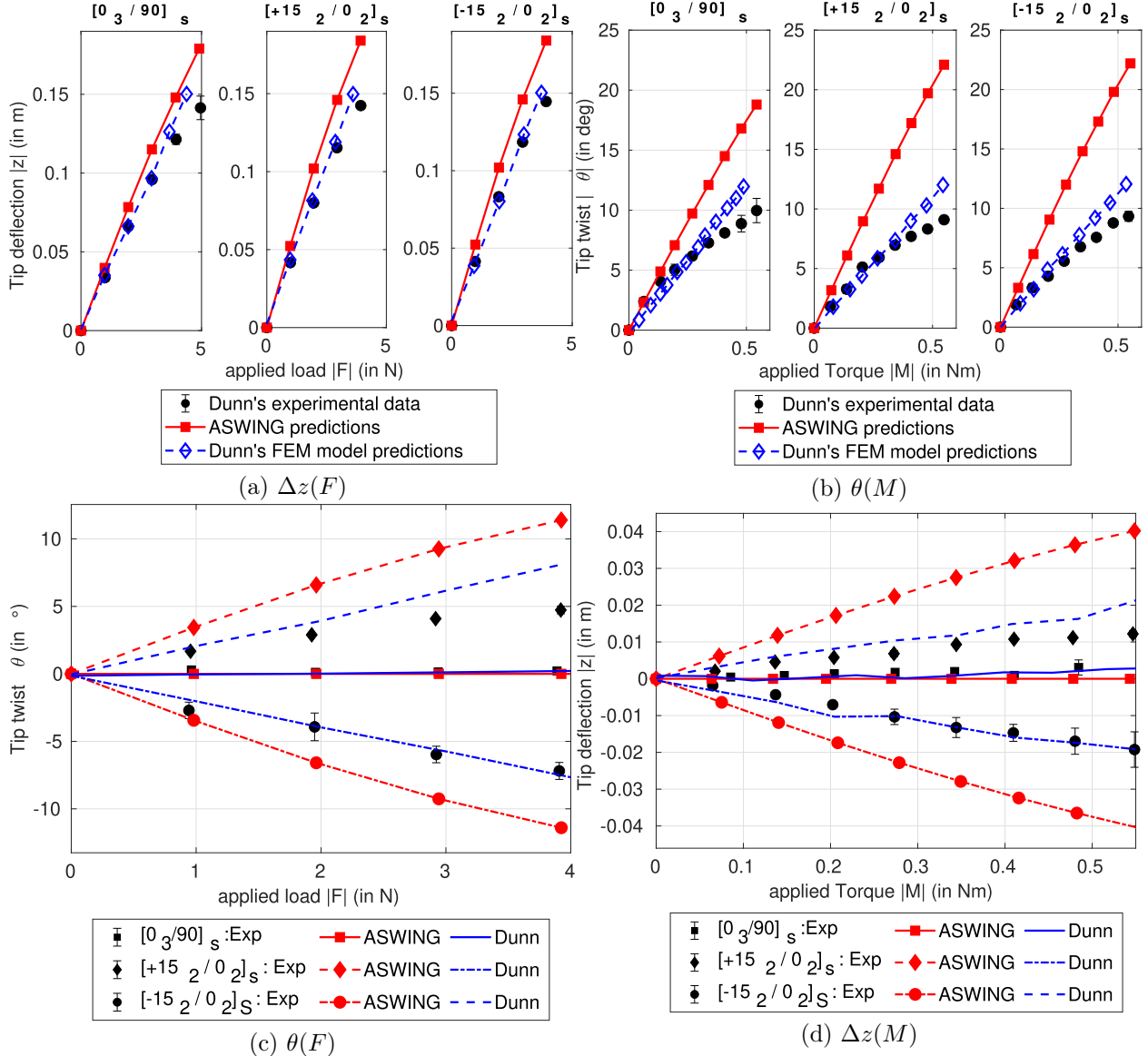


Figure 25: CASE ST-3.A-C: NACA0012 wing static tip deflection and twist against tip forces and moments : ASWING and Dunn's model comparison with experimental data (Dunn -1992)

of particular interest when analysing the effect of a nacelle or wing tip tank on the aeroelastic response of the whole aircraft. To evaluate this feature, the experimental database provided by [Runyan and Sewall \(1948\)](#) has been used. In this note the author provided an experimental analysis of the effect of the spanwise and chordwise position of concentrated weights on the modal response and flutter speed.

CASE ST-4: experimental setup: The tests were carried out in Langley's 4 x 5 ft flutter research wind tunnel. The modal response was performed in a non-flow condition in the wind tunnel. A straight wing was mounted vertically from the top of the section as shown in figure 26. The wing half aspect ratio was 6, providing a good stress test for the Euler-Bernoulli model. The geometrical and structural parameters of the wing are given in the author's work and have been translated into the ASWING formalism and metric system in tab 12. The bending and torsional stiffness were determined experimentally from the static deflection curves of the wing in bending and torsion. Vibrations were recorded using strain gauges attached to the wing as shown in figure 26. The strain gages were connected to a bridge/amplifier cascade system to reduce measurement noise. Frequencies were recorded on an oscilloscope. A total of 100 runs were carried out to ensure that the wing was not structurally damaged from one run to the next, and modal response measurements were taken before and after each run. Based on the results, the author reported that the wing did not suffer any damage throughout the experiment. This was mainly due to the use of wires connected to the wing tip to prevent high deflections when the wing went into flutter. A total of 7 weights with different characteristics were tested, but the 7th will be of particular interest as it varies in span and chord. For ease of reading, weights I-VI have been given the *weights 7a-f* of the technical note [Runyan and Sewall \(1948\)](#). These weights have very close mass properties (constant) as shown in the tab 11. Their index indicates a change in chordwise position. The latter is given as the distance to the elastic axis, denoted as d_W , as shown in figure 26(b)

CASE ST-4: numerical setup: In view of the ASWING formalism, it is not possible to model a concentrated mass, since it has a non-zero inertia tensor. For this purpose, a mass dipole was used, equidistant from the centre of gravity of the concentrated mass at a distance r_W (see figure 26-b). The point mass was half the concentrated mass. The distance r_w , i.e. the radius of gyration, is calculated to recover the concentrated mass inertia. Its numerical values are given in the tab 11. As the weights were designed to have a minimum aerodynamic pressure (symmetrical and slender), we believe that the use of a mass dipole

was the best option to virtually recover the behaviour of a concentrated mass. Once this was decided and implemented, the modal analysis was carried out using the same numerical protocol described in the previous sections.

CASE ST-4: Results: The figures 27 (a) and (b) show an illustrative comparison between experiments and ASWING predictions of the effect of the span size position of a concentrated mass on the first bending and torsion mode frequency. The more the weight is placed towards the wing tip, the lower these mode frequencies will be. The table 6 summarises the 3 first mode predictions and the effect of each weight spanwise coordinate. The results are presented in this way because the results are quite untraceable on a graph, regardless of the mode considered. For the first mode, ASWING captures well the effect of the spanwise position on its frequency. The latter tends to decrease linearly as the weight moves towards the wing tip. The chordwise position (weight index) has no effect. For the second bending mode, ASWING again captures the weight position effect with slightly less accuracy than for the first mode. The mode decreases from 0 to 40% of the half span, then increases between 40 and 70% and finally decreases to the wing tip. Throughout the wing, the second bending mode remains lower than in the configuration where the weight is placed at the wing root. Finally, the torsional mode prediction captures a "tendency" of the weight effect, which is a decrease with weight location. However, the prediction errors are larger than for the previous modes. Despite the low aspect ratio of this case, ASWING is able to capture the effect of concentrated weights on its modal response reasonably well.

4.5 CASE ST-5.A-B: Joined wings

Among the features of Aswing there is the joint connection. Beams can be connected through distant or close compliant/rigid joints. This feature is a of particular interest as it allows the study of joined or diamond wings aeroplanes. A series of work in the 80's and 90's have shown that the main advantage of joined wings is to provide considerable wing mass saving. Indeed, the structure of a joined wing, when its joint location is wisely chosen, take more advantage of the normal bending stiffness of the wing box. It allows the reduction of the wall thickness and thus a mass saving. [Kroo et al.](#) has showed for example that a 40% saving is possible in comparison to a cantilever swept wing with an horizontal stabilizer, leading to a significant fuel saving. Wing boxes walls are mostly designed to resist out of plane bending and vertical shear forces ([31]). Capturing the effect of a joint on

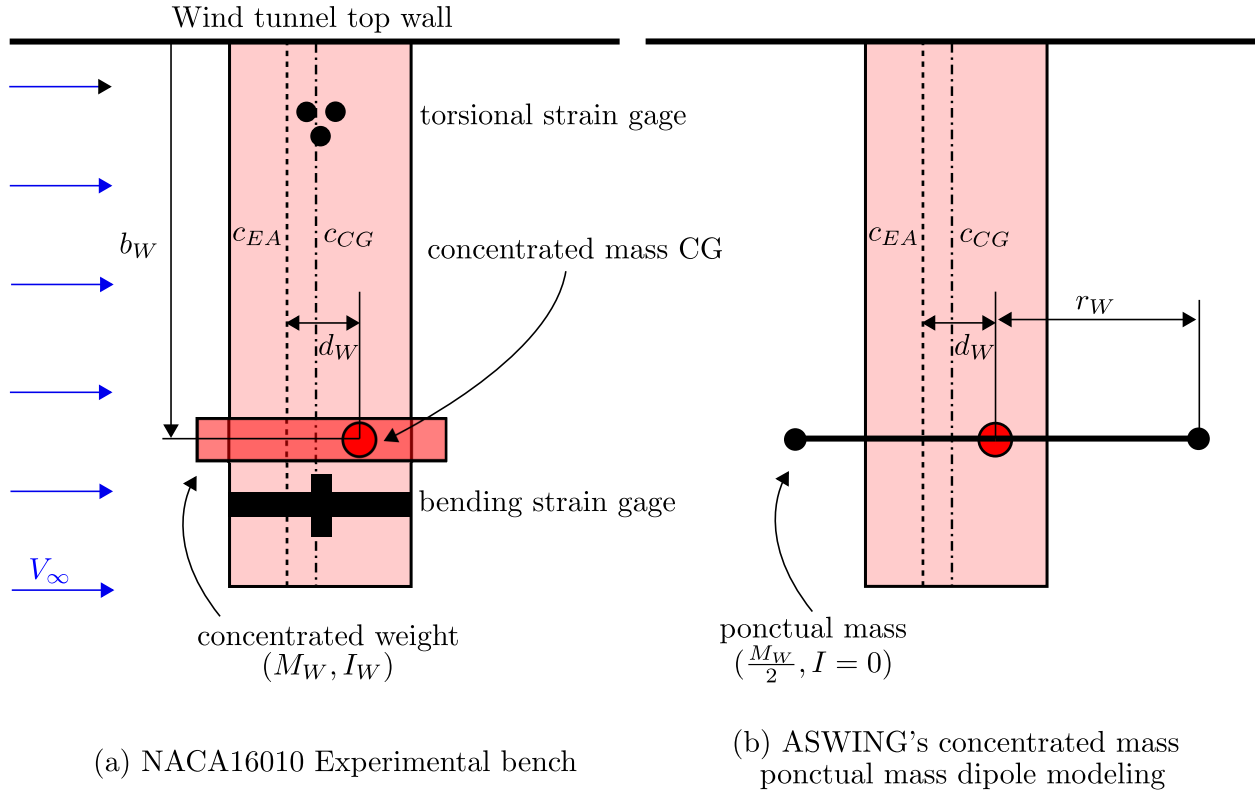


Figure 26: CASE ST-4: concentrated mass effect bench Runyan and Sewall (1948)

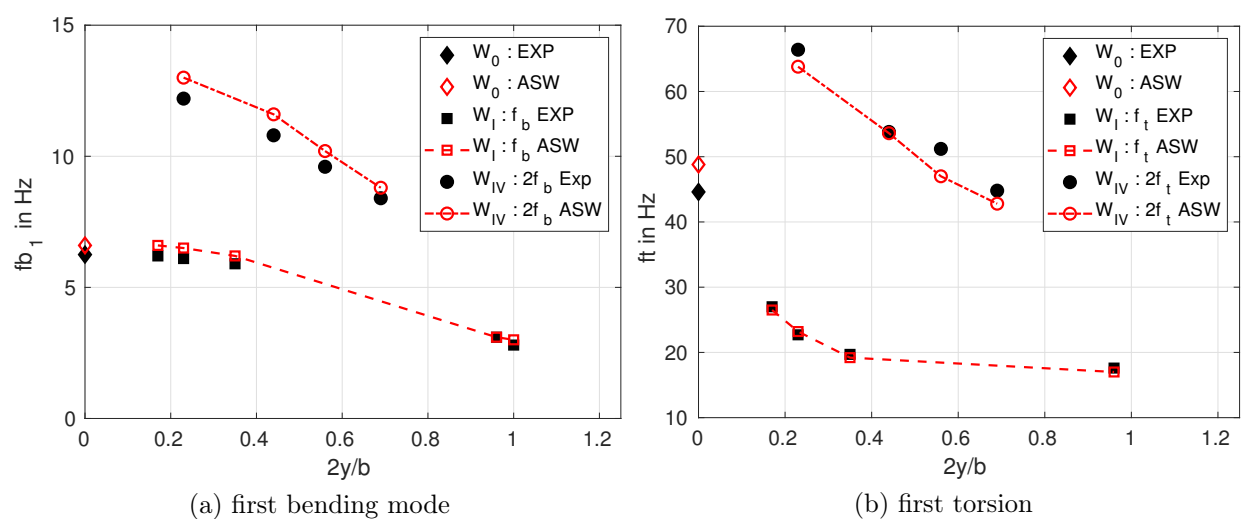


Figure 27: CASE ST-4: Concentrated weight effect on the first bending and torsion modes. ASWING predictions against experiments from Runyan and Sewall (1948).

those quantities, and their variation with the spanwise coordinate is of interest in aircraft design. In this case, the validation of Aswing is proposed using the experimental data of Lin et al.. In their work, they have studied the static response of the NASA-JWRA joined wing 1/6 scale prototype, with different load cases. This geometry is similar to the aerodynamic cases presented in the first part of this evaluation work (cases *SA* – 15 A to C). Lin et al. has studied up to 8 different joints allowing different degrees of freedom. In this work, only two of them are presented that are the rigid and in-the-plane link joints. Those in particular, because they were the one presenting most important differences in performances and also the easiest one to extract the data from. The rigid joint is denoted CASE *ST*-5.A while the in-the-plane link joint is named CASE *ST*-5.B

CASE *ST*-5.A-B: Experimental bench

The geometry is a diamond wing, with the forward wing having a 5° dihedral angle and a 30° swept back angle. The wing is tapered with root and tip chord lengths respectively equal to 0.5638 and 0.2252 ft (0.1718 and 0.06864 meters). The wing span is 6.67 ft (2.03 meters) with an aspect ratio of 13. The JWRA prototype is composed also of a rear wing having a -20° dihedral angle and -32° swept forward angle. The wing is tapered with root and tip chord lengths respectively equal to 0.2476 and 0.1484 ft (0.07548 and 0.04523 meters). The wing span is 4 ft (1.21 meters) and is fixed to the forward wing at 60% of its span. The rear wing aspect ratio is 16. The 2 wings structural boxes parameters (mass, stiffness, inertia etc) are coarsely describe in Lin et al.'s work (cf table 2.1 of his article), with only 3 spanwise discretization for the forward wing, and two for the rear wing. Discrepancies in Aswing prediction could come from the interpolation performed by the software. In total four load cases have been studied. Thirty pounds (13.5 kg) only on the forward wing, corresponding to a cantilever wing. The same load, but with forward wing carrying 90% of it and the rest for the rear. The two other load cases are 20 pounds (9.1 kg) with 90%-10% and 80%-20% load distribution. For every cases, the load distribution was following a cosine function in the spanwise coordinate as illustrated in figure 28-(a). The loads were produced using a system of pulleys at equally spaced spanwise location, with the tension fixed to recover the cosine function integrated on each segment. Finally the loads were applied the elastic axis of each boxes (that is mid-chord). Out of plane bending moments on each wing were measured at different spanwise location, using differential strain gauges. The measurements were performed on the upstream axis (x -axis in figure 28). Regarding the joints, the rigid one corresponds to a connection where all rotations and translations are matched between

the forward and rear wing connection points. The in-the-plane link joint consist of allowing x and y translations as-well as a z rotation. In consequence, only z translations, x and y rotations are matched. This can be performed through the use of two pivot joints connected between them with a in-the-plane linear rail mechanism as depicted in figure 29.

CASE *ST*-5.A-B: Numerical bench

The numerical bench of this case has been built using the second linear mass and inertia distribution parameters of Aswing to reproduced the external cosine load. The mass was set negative to reproduce the aerodynamic load, artificially created by the pulley system. Apart from that, the file is very similar to the above cases. Rigid and compliant joints are natively encoded in Aswing, however they can only be rigid or fully compliant on every axis (either every translations , or rotations matched). A hinge implementation exists but it is not fitted to CASE *ST*-5.B. A modification of the code must have been brought in order to be able to model such joints.

CASE *ST*-5.A-B: Results:

Aswing predictions for the **rigid joint** of the out of plane bending moment projected on x -axis ($M_x(y)$) are presented in figure 28 (b) to (d) for each load cases. As illustrated, no matter the cases, Aswing presents good agreements with the experiments, no matter the spanwise coordinate. It captures well the effect of the joint on the significant reduction of the root bending moment as illustrated in the figures. Same conclusions are done for the rear and the cantilever wing. The JWRA prototype was having a mass around 5kg, or the two load cases are greater corresponding to at least a 2.5G case. The predictions quality is constant with the load case, so Aswing will be suited for structural failure analysis and joined wing box design. As it has been shown in the first part of this experimental validation, Aswing is able to predict well, both the aerodynamic longitudinal and structural characteristics, making it a good candidate for joined wing aircraft design. Moreover according to figures 29 (a) to (c) Aswing also captures with the same level of agreements, the effect of compliant joints such as the **in-the-plane link joint** on the static response of a joined wing, and so no matter again the load cases. In those figures, the major drawbacks brought by this compliant joint can be highlighted. Because of the in-the-plane unmatched translation, the rear wing is no longer working as a strut, and cannot relieve the forward wing bending moment. Moreover Because of the free rotation on the z -axis, the forward and rear wing bending moments can not balanced each other as effectively as for the rigid joint case. Thus the structure of the joint wing is as efficient as a cantilever layout, making the first one irrelevant.

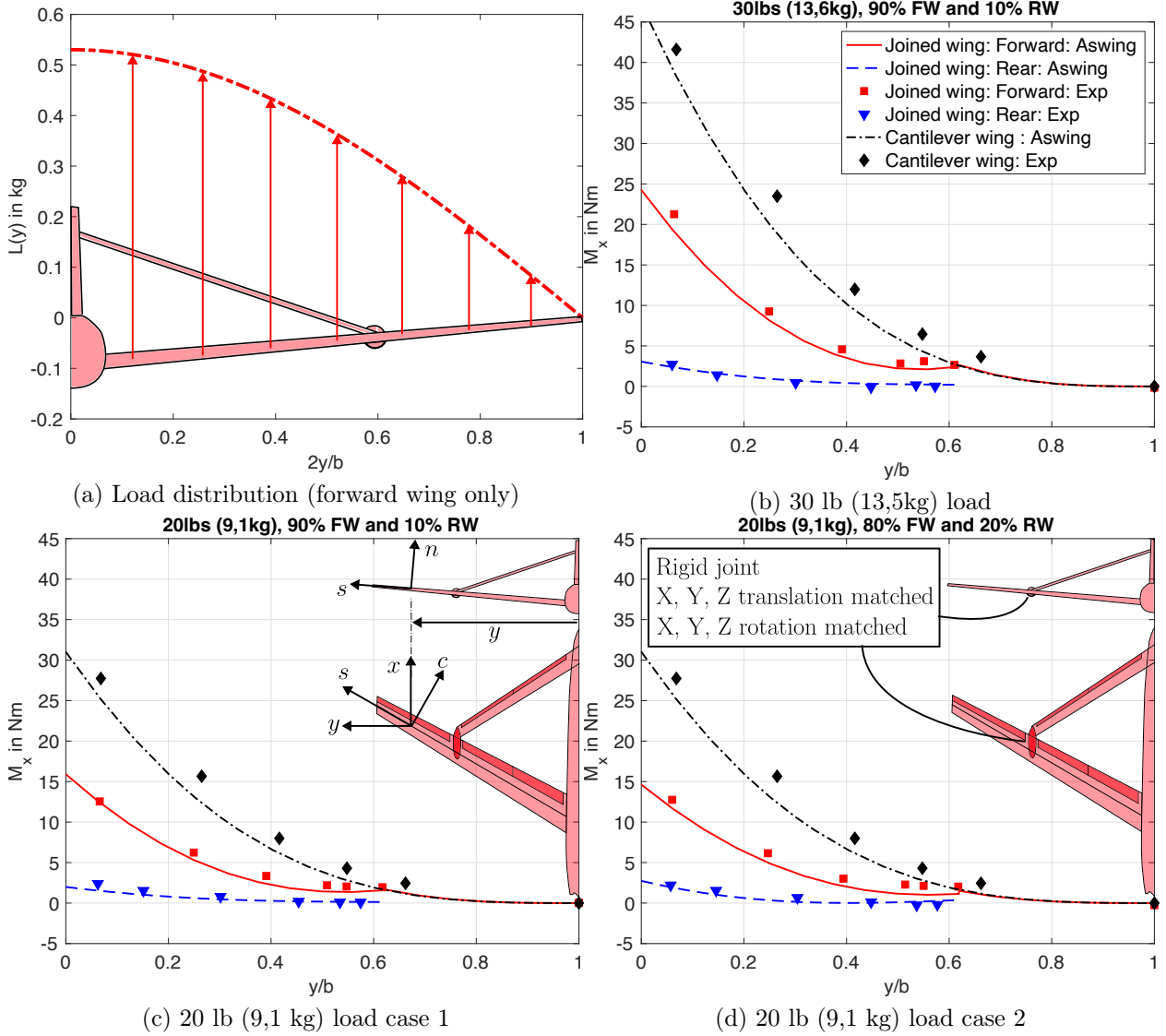


Figure 28: CASE ST-5.A: Joined wing, out of plane bending moment ASWING predictions against experiments of Stearman and Lin et al. (1990). Effect of a **rigid joint** against a cantilever wing. Effect of the load fraction carried by both wings. For figures (c) and (d) experimental data have been extrapolated from the 30 lbs load case.

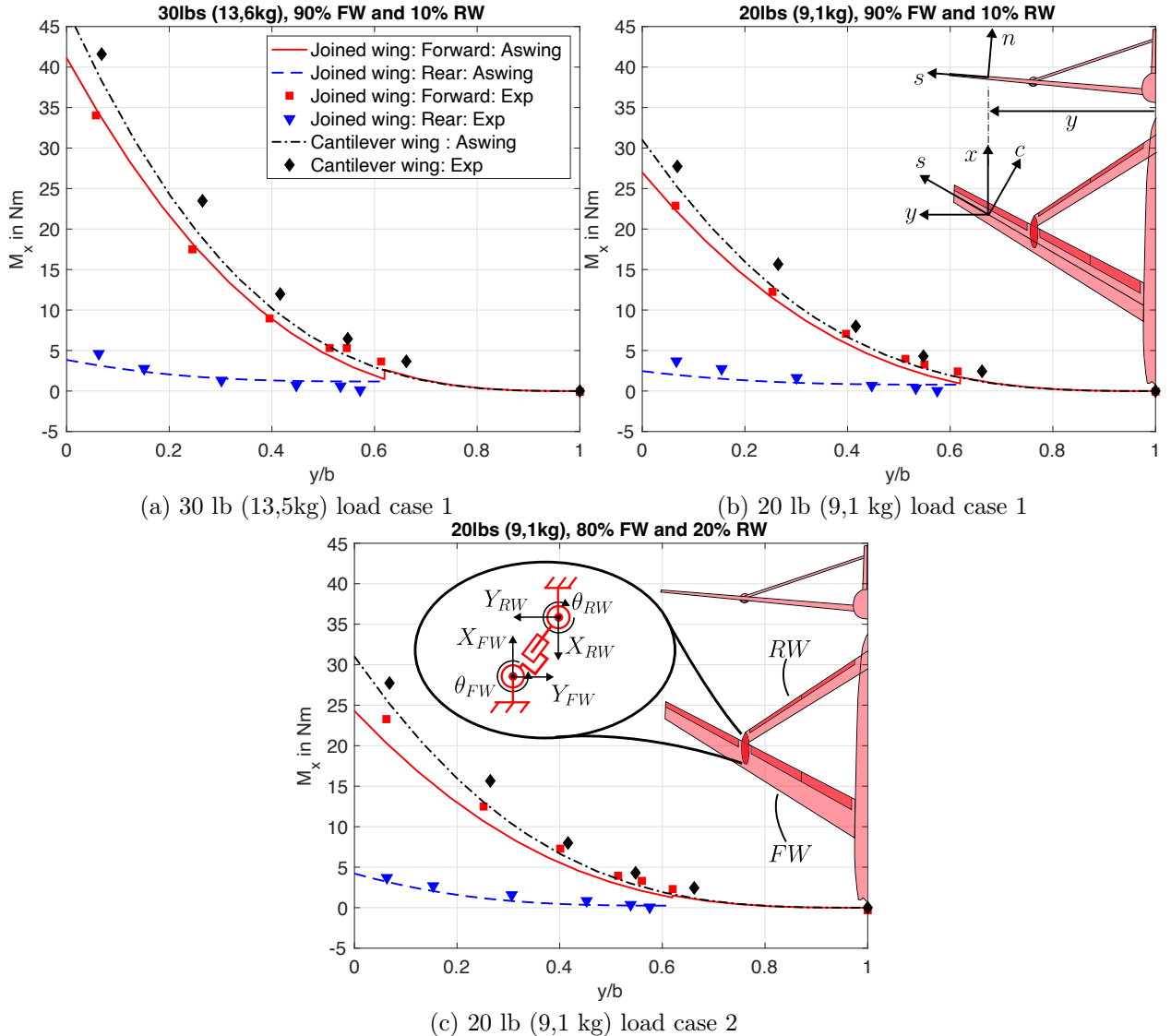


Figure 29: CASE ST-5.B: Joined wing, out of plane bending moment ASWING predictions against experiments of Stearman and Lin et al. (1990). Effect of a **link joint** against a cantilever wing. Effect of the load fraction carried by both wings. For figures (b) and (c) experimental data have been extrapolated from the 30 lbs load case.

4.6 CASE ST-6.A-E Column buckling

As it was seen in the theoretical section, Aswing is able to predict buckling of any type of beams (uniform or not). Yet its precision for this phenomena is not known. This validation case, is particular, as it is not a direct validation. Indeed most of the column buckling test consist of placing a beam of a given length under a high load press. Each beam ends are pinned and are only free to rotate, or not. The problem in Aswing is that it is not possible to have a beam connected to 2 ground points to reproduce the above bench. Instead the upper end of the beam is free, and a tip mass can be applied to reproduce the axial load. The problem with this modeling technique is that it lead to discrepancies because of the different degree of freedom of one of the ends. A modification of the code could be brought in order to solve it, but it will be pointless for aeroelasticity applications. It is important to note that the pinned-pinned cantilevering is possible as it has been seen in the joined wing case. The typical buckling test presented earlier is just not possible to be reproduced.

Unfortunately, the latter is the one providing the widest and numerous range of experimental data. As Aswing's structural model is a non linear extension of the Euler Bernoulli beam theory, the predictions accuracy for buckling critical load calculations are recalled here. To do so, the experimental work of Niles is used here. In their work, they have placed under a press, 5 different beams having various cross section (angle, zee, bar and rod). The latter are illustrated with their dimensions in figure 30. The beams are all made of aluminium alloy (14S-T), with an elastic modulus of 10,6E6 psi ($7.3E10Nm^{-2}$). For such cantilever configuration, the Euler analytical critical load is given by

$$F_{cr} = A \frac{\pi^2 E}{(KL/\rho)^2} \quad (48)$$

where E is the elastic modulus, K is the effective length factor set to 0.5 in this case, ρ is the minimum cross section radius of gyration, L is the length of the beam and, finally A is the cross section area. The ratio, KL/ρ is known to be the effective slenderness ratio, and is useful to detect the weakness of the Euler solution to predict the buckling load. The figure 30 (a) to (d) present a comparison, of the Euler critical load prediction with experimental measurements on the 5 beams. The latter have been denoted as cases $ST - 6.A - E$. The critical load is presented against the effective slenderness ratio, where the radius of gyration ρ is held fixed, and the length of the beam is varying. The Euler solution (and so by extension Aswing), gives good agreements with the experiments as long as the effective slenderness ratio is above 50, and so no matter the cases. The agreements of the

Euler solution also confirm the hypothesis of considering only the minimum radius of gyration (ie minimal cross-section bending stiffness) for such analysis, as the cases B, C and D presenting important difference in the in-the-plane bending stiffness do not show significant prediction error change. It is important to note, that Aswing does not neglect stiffer bending component in its modal analysis, in consequence, more complex buckling cases can be considered where lateral loads or bending moments can be involved such as it can happen on diamond/joined or strut braced wing. In consequence, the effective slenderness ratio can be used as an accuracy indicator for Aswing. As long it is greater than 50, Aswing will provide good predictions of the critical buckling load of a structure. If the previous validation case is considered (Case $ST5$) with the rear wing subject to compression, the slenderness ratio computed based on the bigger cross section (conservative) is equal to 58 which is above the recommended value. Aswing can be used in consequence to assess the buckling property of this specific case. If the slenderness ratio is below 50 there exist a modified version of the Euler solution called the Engesser equation. The reader can find a good explanation of it in Peery's book (*chapter 14, section 14.4 equation 14.16*). This Engesser's solution is not really convenient for the Aswing beam formalism, as it is a direct solution. Instead, a modification that could be brought to the code, would be to have a stall function for the Elastic Young modulus. Unfortunately, the latter is very dependant on the structure material. Such a model exists and is known as the Ramberg-Osgood equation, or the dimensionless form of tangent modulus curves (*cf chapter 14, section 14.8, equation 11.19 of [45]*), dropping the accuracy indicator value to 10. This, once implemented would provide Aswing the same level of accuracy as the one presented in Peery's work (*cf chapter 14, section 14.4, figure 14.7*).

Global not local buckling:

Aswing is able to predict the global buckling of a beam. The local skin buckling for example is not captured. From the bending and shear forces computed from the model, it is possible to detect it with a shear flow analysis code such as Co-Blade but it is not implemented natively in Aswing.

In conclusion, Aswing is able to predict the global divergent buckling of complex structure having a slenderness ratio above 50. It will be most likely the case, as modern aircraft, tends to high aspect ratio layouts increasing the accuracy indicator. As the critical load decreases rapidly with it, such aeroplanes are very likely to be subject to buckling. It is thus highly recommended to perform such analysis in conceptual design loops.

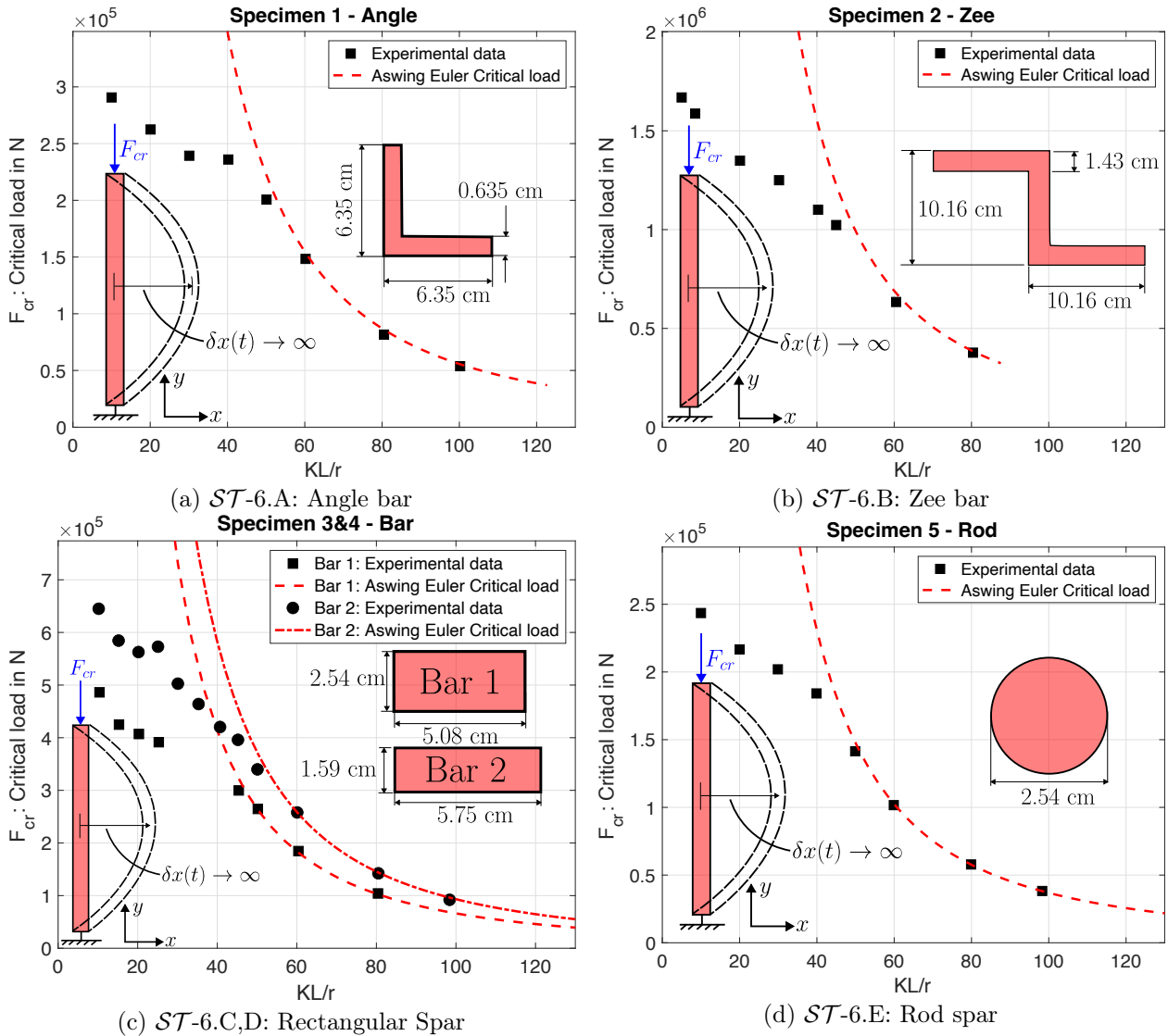


Figure 30: CASE ST-6.A-E: Column buckling validation cases, with various cross section. Effect of the effective slenderness ratio KL/r (with $K = 0.5$) on the critical load. Aswing expected predictions performance based on the Euler critical load solution. Experiments are from Niles's technical note.

5 Conclusion:

An experimental evaluation of the ASWING structural model was presented in this report. The focus was on static deflections, modal response and the effect of concentrated weights and joint on these. The experimental cases were chosen to be as stressful as possible. In the light of the results, the following findings can be summarised

- The mesh convergence study for tip deflection and modal response predictions shows that only 40 structural nodes clustered by a cosine function are sufficient to provide converged results. Using this, the computation times on a modern laptop for a single tip deflection and modal analysis are 0.250 s and 2.0 s respectively. When point solutions are near, the computation time drops to 0.100 and 1.0 seconds, respectively.
- ASWING shows excellent agreement with experiments for high aspect ratio beams. In particular, the non-linear 3D high deflections are well captured. The modal predictions of the first 5 modes are also good. Neglecting some of the extensional/bending terms shows no effect on the tip deflection predictions and modal response.
- The Pazy wing bench has been used to stress ASWING for moderate aspect ratio. The latter still shows good agreement with experiments for tip deflection, while for torsion it starts to get weaker at high deflections. The mode frequency predictions are in excellent agreement with the experiments. Overall, ASWING can still be used for this type of layout.
- Three low aspect ratio cases have shown the weakness of the model in predicting tip deflections. The use of a strong tip loads seems to involve effects that are not captured by ASWING. As the aerodynamic loads are much more scattered along the beam, fewer discrepancies are expected. Tip pontual load benches could not be well adapted for aeroelasticity evaluation.
- ASWING can also capture well the effect of concentrated weights in spanwise and chordwise positions on the modal response of a wing. This last feature is of particular interest when it comes to study the tank or nacelle position effect on the flutter response of a wing.
- The beam model has been shown to be a good candidate for joined wing boxes design, as it predicts well the out of plane bending moment distribution of each wing in high load condition.

The effects of rigid and compliant joints on the load distribution are also well captured.

- Aswing is able to predict the global divergent buckling of complex structure having a slenderness ratio above 50. It will be most likely the case, as modern aircraft, tends to high aspect ratio layouts increasing the accuracy indicator.

Note that structural viscous damping has not been evaluated. This has been done by [Banks and Wang \(1987\)](#) but for a small pinch time marching response. An experimental campaign should be considered to evaluate this last feature. Also, with the advent of modern sensors, modal shape response measurements should be considered and compared with the ASWING predictions.

N_W	ew	y/b	$f_{b1_{exp}} \text{ (Hz)}$	$f_{b1_{ASW}} \text{ (Hz)}$	$\epsilon \text{ (%)}$	$f_{b2_{exp}}$	$f_{b2_{ASW}}$	ϵ	$f_{t_{exp}}$	$f_{t_{ASW}}$	ϵ
I	0	0	6.25	6.6	5.9	35.8	40.54	13.2	44.6	48.8	9.59
	0.17	6.2	6.6	5.9	36	36.5	1.4	27	26.5	-1.6	
	0.23	6.1	6.5	6.7	35	34.6	-1.3	22.7	23.2	2.0	
II	-0.818	0.35	5.9	6.2	5.0	NC	31.5	19.7	19.2	-2.45	
	0.96	3.1	3.1	0	31.7	33.3	5.0	17.6	17	-3.4	
	1	2.8	3.0	7	29.8	31.3	5.0	NC	16.8		
III	-0.578	0.23	6.1	6.5	6.2	25.6	28	9.5	33.6	38	13
	0.44	2.3	5.8	9.6	25.0	21.6	-13.6	28	33	33	17
	0.23	6.2	6.5	5.7	26.7	27.6	3.5	34.5	32.9	-4.6	
IV	-0.360	0.44	5.4	5.8	8.0	22.5	22.2	-1.2	27	28.8	4.8
	0.58	4.6	5.0	8.0	29.4	30.4	3.6	23.1	21.8	-5.8	
	0.23	6.1	6.5	6.8	24.5	29.3	19.7	33.2	31.9	-4.0	
V	-0.140	0.44	5.4	5.8	7.4	23.2	24.3	4.8	26.1	26.8	2.5
	0.56	4.8	5.1	7.0	27.4	28.6	4.5	25.6	23.5	-8.4	
	0.69	4.2	4.4	4.9	34.2	39.1	14.1	22.4	21.4	-3.9	
VI	0.23	6.3	6.5	3.6	26.7	29.6	10.8	37.4	31.6	-15.4	
	0.44	5.6	5.8	4.4	29.4	25.6	-12.8	29.1	25.2	-13.5	
	0.60	4.7	4.9	4.3	30	30.2	0.8	25.3	23.1	-8.5	
	0.72	4.0	4.2	3.6	35.6	37.7	5.7	30.0	21.9	-26.9	
	0.83	3.6	3.6	0.0	34.6	38.5	11.4	22.7	21.1	-7.2	
	0.23	6.2	6.5	4.9	38.3	33.8	NC	36.8	26.7	-27.6	
VII	0.33	6	6.3	4.5	35.3	31.0	-12.1	34.6	22.9	-33.7	
	0.5	5.25	5.82	11	31.7	28.3	-10	26.2	22.2	-15.2	
	0.83	4.4	4.5	3.7	34.2	34.9	2.1	21.5	21.5	0	

Table 6: CASE ST-4: NACA16010 straight wing modal analysis (NC : reported as Not Clear) Runyan and Sewall (1948).
Effect of concentrated weights spanwise and chordwise position on the modal response
 $\epsilon_{\bar{f}b_1} = 5.6 \pm 2.5\%$, $\epsilon_{\bar{f}b_2} = 7.5 \pm 5.3\%$, $\epsilon_{\bar{f}t} = 10.5 \pm 9\%$

References

- [1] Afonso, F., Vale, J., Oliveira, É., Lau, F., and Suleman, A. (2017). A review on non-linear aeroelasticity of high aspect-ratio wings. *Progress in Aerospace Sciences*, 89:40–57.
- [2] Avin, O., Raveh, D. E., Drachinsky, A., Ben-Shmuel, Y., and Tur, M. (2022). Experimental aeroelastic benchmark of a very flexible wing. *AIAA Journal*, 60(3):1745–1768.
- [3] Banks, H. T. and Inman, D. J. (1991). On Damping Mechanisms in Beams. *Journal of Applied Mechanics*, 58(3):716–723.
- [4] Banks, H. T. and Wang, Y. (1987). Parameters identification techniques for the estimation of damping in flexible structure experiments. volume TP6 of *Descision and Control Conference*, Los Angeles. Descision and Control Conference.
- [5] Cesnik, C. E., Palacios, R., and Reichenbach, E. Y. (2014). Reexamined structural design procedures for very flexible aircraft. *Journal of Aircraft*, 51(5):1580–1591.
- [6] Chambon, A., Sanches, L., Prothin, S., Eloy, C., and Michon, G. (2022). Structural dynamics of flexible rotor blades to study aeroelastic phenomena. In *AIAA AVIATION 2022 Forum*, Chicago, IL & Virtual. American Institute of Aeronautics and Astronautics.
- [7] Chau, T. and Zingg, D. W. (2022). Aerodynamic design optimization of a transonic strut-braced-wing regional aircraft. *Journal of Aircraft*, 59(1):253–271.
- [8] Chauhan, S. S. and Martins, J. R. (2019). Low-fidelity aerostructural optimization of aircraft wings with a simplified wingbox model using open-aerostruct. In *EngOpt 2018 Proceedings of the 6th International Conference on Engineering Optimization*, pages 418–431. Springer.
- [9] Cheung, R. C., Rezgui, D., Cooper, J. E., and Wilson, T. (2020). Testing of folding wingtip for gust load alleviation of flexible high-aspect-ratio wing. *Journal of Aircraft*, 57(5):876–888.
- [10] Clarke, M. A., Erhard, R. M., Smart, J. T., and Alonso, J. (2021). Aerodynamic optimization of wing-mounted propeller configurations for distributed electric propulsion architectures. In *AIAA Aviation 2021 Forum*, page 2471.
- [11] Colas, D., Roberts, N. H., and Suryakumar, V. S. (2018). HALE Multidisciplinary Design Optimization Part I: Solar-Powered Single and Multiple-Boom Aircraft. In *2018 Aviation Technology, Integration, and Operations Conference*, Atlanta, Georgia. American Institute of Aeronautics and Astronautics.
- [12] del Carre, A., Muñoz-Simón, A., Goizueta, N., and Palacios, R. (2019). Sharpy: A dynamic aeroelastic simulation toolbox for very flexible aircraft and wind turbines. *Journal of Open Source Software*, 4(44):1885.
- [13] Drela, M. (1988). Low-Reynolds-number airfoil design for the M.I.T. Daedalus prototype- A case study. *Journal of Aircraft*, 25(8):724–732.
- [14] Drela, M. (1990). Method for simultaneous wing aerodynamic and structural load prediction. *Journal of Aircraft*, 27(8):692–699.
- [15] Drela, M. (1999). Integrated simulation model for preliminary aerodynamic, structural, and control-law design of aircraft. In *40th Structures, Structural Dynamics, and Materials Conference and Exhibit*, St. Louis, MO, U.S.A. American Institute of Aeronautics and Astronautics.
- [16] Drela, M. (2008). ASWING 5.81 Technical Description — Unsteady Extension. page 42.
- [17] Drela, M. (2009). ASWING 5.86 Technical Description — Steady Formulation. page 57.
- [18] Drela, M., Galbraith, M., Haimes, R., Allmaras, S. R., and Darmofal, D. (2019). Hybrid Shell Model for Aeroelastic Modeling. In *AIAA Scitech 2019 Forum*, San Diego, California. American Institute of Aeronautics and Astronautics.
- [19] Dunn, P. (1992). *NONLINEAR STALL FLUTTER of WINGS with BENDING-TORSION COUPLING*. PhD thesis, MIT, Boston, MA.
- [20] Dunn, P. and Dugundji, J. (1992). Nonlinear stall flutter and divergence analysis of cantilevered graphite/epoxy wings. *AIAA Journal*, 30(1):153–162.
- [21] Gallman, J. W., Smith, S. C., and Kroo, I. M. (1993). Optimization of joined-wing aircraft. *Journal of Aircraft*, 30(6):897–905.
- [22] Gilbert, C., Armstrong, B., Johansson, O., Squibb, C., and Philen, M. (2023). Control of a Flapping Plate Shape with Fluidic Flexible Matrix Composites. In *AIAA SCITECH 2023 Forum*, National Harbor, MD & Online. American Institute of Aeronautics and Astronautics.
- [23] Goizueta, N., Wynn, A., Palacios, R., Drachinsky, A., and Raveh, D. E. (2022). Flutter predictions for very flexible wing wind tunnel test. *Journal of Aircraft*, 59(4):1082–1097.

- [24] González, O., Boschetti, P., Cárdenas, E., and Amerio, A. (2010). Static-Stability Analysis of an Unmanned Airplane as a Flexible-Body. In *AIAA Atmospheric Flight Mechanics Conference*, Toronto, Ontario, Canada. American Institute of Aeronautics and Astronautics.
- [25] Gu, H., Healy, F., Rezgui, D., and Cooper, J. (2023). Sizing of high-aspect-ratio wings with folding wingtips. *Journal of Aircraft*, 60(2):461–475.
- [26] Healy, F., Cheung, R., Rezgui, D., Cooper, J., Wilson, T., and Castrichini, A. (2023a). Experimental and numerical nonlinear stability analysis of wings incorporating flared folding wingtips. *Journal of Aircraft*, pages 1–15.
- [27] Healy, F., Courcy, J. D., Gu, H., Rezgui, D., Cooper, J., Wilson, T., and Castrichini, A. (2023b). On the dynamic behavior of wings incorporating floating wingtip fuel tanks. *Journal of Aircraft*, pages 1–16.
- [28] Jones, J. (2017). *Development of a very flexible testbed aircraft for the validation of nonlinear aeroelastic codes*. PhD thesis.
- [29] Jonsson, E., Riso, C., Lupp, C. A., Cesnik, C. E., Martins, J. R., and Epureanu, B. I. (2019). Flutter and post-flutter constraints in aircraft design optimization. *Progress in Aerospace Sciences*, 109:100537.
- [30] Krengel, M. D., Hepperle, M., and Huebner, A. (2019). Aeroviscoelastic Wing Sizing Using a Physics-Based Approach in Conceptual Aircraft Design. In *AIAA Aviation 2019 Forum*, Dallas, Texas. American Institute of Aeronautics and Astronautics.
- [31] Kroo, I., Gallman, J., and Smith, S. (1991). Aerodynamic and structural studies of joined-wing aircraft. *Journal of aircraft*, 28(1):74–81.
- [32] Landsberger, B. J. (1983). AEROELASTIC PROPERTIES OF STRAIGHT AND FORWARD SWEPT GRAPHITE/EPOXY WINGS.
- [33] Landsberger, B. J. and Dugundji, J. (1985). Experimental aeroelastic behavior of unswept and forward-swept cantilever graphite/epoxy wings. *Journal of Aircraft*, 22(8):679–686.
- [34] Lehoucq, R. B., Sorensen, D. C., and Yang, C. (1998). *ARPACK Users' Guide: Solution of Large-Scale Eigenvalue Problems with Implicitly Restarted Arnoldi Methods*. Society for Industrial and Applied Mathematics.
- [35] Lin, H.-H., Jhou, J., and Stearman, R. (1989). Influence of joint fixity on the structural static and dynamic response of a joined-wing aircraft: Part i: Static response. *SAE Transactions*, pages 221–234.
- [36] Love, M., Zink, P., Wiesemann, P., and Younghren, H. (2005). Body Freedom Flutter of High Aspect Ratio Flying Wings. In *46th AIAA/ASME/ASCE/AHS/ASC Structures, Structural Dynamics and Materials Conference*, Austin, Texas. American Institute of Aeronautics and Astronautics.
- [37] Minguet, P. and Dugundji, J. (1990a). Experiments and analysis for composite blades under large deflections. I - Static behavior. *AIAA Journal*, 28(9):1573–1579.
- [38] Minguet, P. and Dugundji, J. (1990b). Experiments and analysis for composite blades under large deflections. II - Dynamic behavior. *AIAA Journal*, 28(9):1580–1588.
- [39] Minguet, P. J. (1989). *Static and Dynamic Behavior of Composite Helicopter Rotor Blades under Large Deflections*. PhD thesis, MIT, Boston, MA.
- [40] Niles, D. E. (1946). Column and plate compressive strengths of aircraft structural materials: Extruded 14s-t aluminum alloy. Technical Report Technical note 1027, NACA.
- [41] Ning, S. A. and Kroo, I. (2010). Multidisciplinary considerations in the design of wings and wing tip devices. *Journal of aircraft*, 47(2):534–543.
- [42] Otsuka, K. and Makihara, K. (2019). Absolute Nodal Coordinate Beam Element for Modeling Flexible and Deployable Aerospace Structures. *AIAA Journal*, 57(3):1343–1346.
- [43] Patil, M. J., Hodges, D. H., and Cesnik, C. E. (2001a). Limit-cycle oscillations in high-aspect-ratio wings. *Journal of fluids and structures*, 15(1):107–132.
- [44] Patil, M. J., Hodges, D. H., and Cesnik, C. E. (2001b). Nonlinear aeroelasticity and flight dynamics of high-altitude long-endurance aircraft. *Journal of Aircraft*, 38(1):88–94.
- [45] Peery, D. J. (2011). *Aircraft structures*. Courier Corporation.
- [46] Riso, C. and Cesnik, C. E. (2023). Impact of low-order modeling on aeroelastic predictions for very flexible wings. *Journal of Aircraft*, 60(3):662–687.
- [47] Runyan, H. L. and Sewall, J. L. (1948). Experimental investigation of the effects of concentrated weights on flutter characteristics of a straight cantilever wing. NACA Technical Note 1594, NACA, Langley Memorial Aeronautical Laboratory, Langley Field.

- [48] Sinha, A. (2021). Free Vibration of an Euler–Bernoulli Beam with Arbitrary Nonuniformities and Discontinuities. *AIAA Journal*, 59(11):4805–4808.
- [49] Stearman, R. (1990). Influence of joint fixity on the aeroelastic characteristics of a joined wing structure. In *31st Structures, Structural Dynamics and Materials Conference*, page 980.
- [50] Su, W. and Cesnik, C. E. (2010). Nonlinear aeroelasticity of a very flexible blended-wing-body aircraft. *Journal of Aircraft*, 47(5):1539–1553.
- [51] Uranga, A., Drela, M., Greitzer, E. M., Hall, D. K., Titchener, N. A., Lieu, M. K., Siu, N. M., Casses, C., Huang, A. C., Gatlin, G. M., et al. (2017). Boundary layer ingestion benefit of the d8 transport aircraft. *AIAA journal*, 55(11):3693–3708.
- [52] Variyar, A., Economou, T. D., and Alonso, J. J. (2017). Design and Optimization of Unconventional Aircraft Configurations with Aeroelastic Constraints. In *55th AIAA Aerospace Sciences Meeting*, Grapevine, Texas. American Institute of Aeronautics and Astronautics.
- [53] Wang, X. and Xia, P. (2022). Novel Modeling and Vibration Analysis Method on a Helicopter Drive Train System. *AIAA Journal*, 60(7):4288–4301.
- [54] Warwick, S., Bras, M., Richards, J., and Suleiman, A. (2019). Measurement of Aeroelastic Wing Deflections Using Modal Shapes and Strain Pattern Analysis. In *AIAA Scitech 2019 Forum*, San Diego, California. American Institute of Aeronautics and Astronautics.
- [55] Willis, D., Israeli, E., Persson, P.-O., Drela, M., Peraire, J., Swartz, S., and Breuer, K. (2007). A Computational Framework for Fluid Structure Interaction in Biologically Inspired Flapping Flight. In *25th AIAA Applied Aerodynamics Conference*, Miami, Florida. American Institute of Aeronautics and Astronautics.

Appendix

The tables 7-9 provides the helicopter blades properties. The properties of the first 4 laminates can be found in the table 5.1 p 100 while the fifth in Table 5.2(a) p 124 of [Minguet \(1989\)](#). The table 10 provides the properties of the laminates of CASE ST-3. Data from *Appendix B page 175* of [Dunn's PhD script \(1992\)](#) were used and translated to the Euler-Bernoulli formalism. Mass/length and inertia/length were not provided and so were deducted from the material properties given in *Appendix A page 173-174* of [Dunn's work \(1992\)](#). The tables 11 and 12 provide the wing and weight properties of CASE ST-4. The weights values are taken from *Table I page 8* and the wing ones are given on *page 4* of [Runyan and Sewall \(1948\)](#)'s technical report. Data is translated from the imperial to the metric system.

Laminate	GKc	EA	GKn	E_{12}	E_{25}
Unit	N	N	N	N	Nm
[0/90] _{3s}	2.6E5	3.7E6	2.9E5		
[45/0] _{3s}	2.6E5	4.0E6	5.5E5	2.7E5	
[20/ - 70/ - 70/20] _{2a}	1.1E6	3.9E6	1.210E5		5.22E2
[45/0] _{3a}	8.7E5	3.7E6	2.2E6		2.26E2
[45/0] _s	2.7E5	1.3E6	1.0E5	9E4	

Table 7: CASE ST-1: helicopter blades: properties 1/3 Minguet (1989)

Laminate	$EIcc$	GJ	$EIcs$	E_{45}
Unit	Nm^2	Nm^2	Nm^2	Nm^2
[0/90] _{3s}	7.07E-1	1.83E-1	2.76E2	
[45/0] _{3s}	5.22E-1	3.68E-1	2.98E2	1.02E-1
[20/ - 70/ - 70/20] _{2a}	9.83E-1	1.18	2.9E2	
[45/0] _{3a}	5.55E-1	8.54E-1	2.79E2	
[45/0] _s	1.43E-2	1.95E-2	9.9E1	6.32E-1

Table 8: CASE ST-1: helicopter blades: properties 2/3

Laminate	mg	$mgIcc$	$mgInn$	ϑ
Unit	kg/m	kgm	kgm	degrees
[0/90] _{3s}	7.95E-2	1.31E-8	5.3E-6	0
[45/0] _{3s}	6.97E-2	1.25E-8	5.22E-6	0
[20/ - 70/ - 70/20] _{2a}	9.10E-2	2.79E-8	6.82E-6	0
[45/0] _{3a}	6.92E-2	1.22E-8	5.19E-6	65
[45/0] _s	2.38E-2	6.22E-10	1.91E-6	0

Table 9: CASE ST-1: helicopter blades: properties 3/3

Parameters	Units	[0 ₃ /90] _s	[+15 ₂ /0] _s	[+15 ₂ /0] _s
EI_{cc}	N	1.4163	1.2947	1.2947
EI_{nn}	N	$1.8499 \cdot 10^4$	$2.2775 \cdot 10^4$	$2.2775 \cdot 10^4$
EI_{cn}	N	0.0023	0.0021	0.0021
EI_{cs}	N	0	0.5151	-0.5151
GJ	N	1.2	1.2	1.4
EA	N	$1.132 \cdot 10^7$	$1.3944 \cdot 10^7$	$1.3944 \cdot 10^7$
μg	kg/m	0.2310	0.2310	0.2310
$\mu g i_{cc}$	kgm	$9.2385 \cdot 10^{-7}$	$9.2385 \cdot 10^{-7}$	$9.2385 \cdot 10^{-7}$
$\mu g i_{nn}$	kgm	$3.4623 \cdot 10^{-4}$	$3.4623 \cdot 10^{-4}$	$3.4623 \cdot 10^{-4}$
c	m	0.140	0.140	0.140
b	m	0.558	0.558	0.558
AR	m	4	4	4
c_{EA}	m	0.5	0.5	0.5
c_{TA}	m	0.4	0.4	0.4

Table 10: CASE ST-3: NACA0012 wing stiffness and geometry parameters Dunn (1992)

Parameters	M_W	d_w	$I_{W,EA}$	I_W	r_W
Unit	kg	m	kgm^2	kgm^2	m
I	1.4475	-0.0831	0.0185	0.0085	0.0766
II	1.4696	-0.0587	0.0124	0.0073	0.0707
III	1.4838	-0.0366	0.0089	0.0069	0.0680
IV	1.4933	-0.0142	0.0067	0.0064	0.0657
V	1.5059	0.0035	0.008	0.0068	0.0670
VI	1.4475	0.0508	0.0099	0.0061	0.0650

Table 11: CASE \mathcal{ST} -4: NACA16010 wing concentrated weights properties [Runyan and Sewall \(1948\)](#)

Parameters	c	b	AR	λ	μI_{cc}	EI_{cc}	GJ	c_{CG}	c_{EA}
Unit	m	m			kgm	kgm^2	kgm^2	m	m
Value	0.2032	1.2193	6	1	7.8E-3	41.17	20.25	0.0923	0.088

Table 12: CASE \mathcal{ST} -4: NACA16010 wing geometry and structural properties [Runyan and Sewall \(1948\)](#)



Adresse postale
ISAE-SUPAERO
10 avenue É. Belin – BP 54032
31055 Toulouse CEDEX 4 – France

Téléphone
33 (0)5 61 33 80 80

Site internet
www.isae-supaero.fr